Topological sensitivity-based analysis and optimization of microstructured interfaces

Marie Touboul, Rémi Cornaggia, Cédric Bellis

To cite this version:

Marie Touboul, Rémi Cornaggia, Cédric Bellis. Topological sensitivity-based analysis and optimization of microstructured interfaces. Multiscale Modeling and Simulation: A SIAM Interdisciplinary Journal, 2024, 22 (2), pp.836-868. 10.1137/23M1593528 . hal-04180360v3

HAL Id: hal-04180360
https://hal.science/hal-04180360v3

Submitted on 6 Jun 2024

MULTISCALE MODEL. SIMUL.
Vol. 22, No. 2, pp. 836–868

TOPOLOGICAL SENSITIVITY-BASED ANALYSIS AND OPTIMIZATION OF MICROSTRUCTURED INTERFACES*

MARIE TOUBOUL[†], RÉMI CORNAGGIA[‡], AND CÉDRIC BELLIS[§]

Abstract. This paper concerns the optimization of microstructures within a surface when considering the propagation of scalar waves across a periodic row of inclusions embedded within a homogeneous matrix. The approach relies on the low-frequency homogenized model, which consists, in the present case, of some effective jump conditions through a discontinuity within the ambient medium. The topological derivatives of the effective parameters defining these jump conditions are computed from an asymptotic analysis. Their expressions are validated numerically and then used to study the sensitivity of the homogenized model to the geometry in the case of elliptic inclusions. Finally, a topological optimization algorithm is used to minimize a given cost functional. This relies on the expression of the topological derivatives to iteratively perform phase changes in the unit cell characterizing the material, and on FFT-accelerated solvers previously adapted to solve the band cell problems underlying the homogenized model. To illustrate this approach, the resulting procedure is applied to the design of a microstructure that minimizes transmitted fields along a given direction.

Key words. topological optimization, asymptotic methods, periodic media, microstructured interfaces, effective jump conditions

MSC codes. 35, 41, 74

DOI. 10.1137/23M1593528

1. Introduction.

The design of microstructured media allows one to control wave propagation and may lead to exotic effects, e.g., negative refraction, subwavelength imaging, lensing, and cloaking, to cite a few. It constitutes the paradigm of metamaterials, which have undergone spectacular developments since the early 2000s; see [19] and references therein for an overview. An active direction of research concerns the size reduction of microstructures to design compact metamaterial devices. It is indeed advantageous to replace a volumic distribution by a surfacic (in three dimensions) or a lineic (in two dimensions) distribution of scatterers, often called metasurface [10] or metainterface [27].

The two-scale homogenization method is a privileged tool to derive formally an approximate model for wave propagation in microstructured media [12, 44]. It avoids having to mesh fine spatial scales and gives an analytical insight on the macroscopic behavior of waves. However, the usual homogenization methods in the bulk fail when considering a thin row of scatterers, because of boundary effects at the transition between the scatterers and the homogeneous medium in which it is embedded. To recover their efficiency, these methods must then be combined with matched asymptotic expansions [29], yielding effective jump conditions on an equivalent metainterface [21, 31, 20, 30, 42].

---

*Received by the editors August 14, 2023; accepted for publication (in revised form) April 17, 2024; published electronically June 6, 2024.
https://doi.org/10.1137/23M1593528

[†]UMI 2004 Abraham de Moivre-CNRS, Department of Mathematics, Imperial College London, London SW7 2AZ, UK (m.touboul@imperial.ac.uk).

[‡]Sorbonne Université, CNRS, UMR, 7190, Institut Jean Le Rond ∂'Alembert, F-75005 Paris, France (remi.cornaggia@sorbonne-universite.fr).

[§]Aix Marseille Université, CNRS, Centrale Marseille, LMA, Marseille, France (bellis@lma.cnrs-mrs.fr).

In the context of metamaterials, the optimization of microstructures is a useful tool to determine designs that exhibit interesting macroscopic behaviors. To this purpose, different types of optimization can be considered: (i) the *parametric* optimization when the shapes are parameterized by a fixed number of variables (thickness, dimensions, etc.); (ii) the *shape* optimization [1] when, from an initial shape, the position of the boundaries of the microstructure is changed without changing its topology; (iii) the *topological* optimization [11] when the best possible geometry is sought, even if it means changing the topology. In this work, we are interested in topological optimization, which leaves more freedom compared to the first two methods. The chosen mathematical tool to perform this type of optimization is the *topological derivative* [7, 38], which measures the sensitivity of a cost functional to infinitesimal topological perturbations.

Then, different numerical methods can be employed to update the material properties based on the knowledge of the topological derivatives. One method used in this paper is the *level-set* method. For a two-phase material, it relies on the characterization of the phase distribution thanks to a level-set function which is strictly positive in one phase and strictly negative in the other phase. This was first introduced for *shape* optimization and is based on the fact that the interface between phases, which corresponds to the zero level-set function, can evolve based on the shape derivative of the cost functional with respect to a perturbation of this interface [2, 3]. This methodology was then adapted to topological perturbations based on a projection algorithm [8, 9, 24, 39].

A strategy for microstructure optimization, in line with the homogenization setting considered in this paper, is to perform the optimization from the homogenized model that describes the material, an issue often referred to as inverse homogenization [45]. It relies on the definition of a cost function, to be minimized, in terms of the effective coefficients that characterize the homogenized model. At low frequency, this method has been used in statics [9, 25, 39] and in dynamics for a low contrast [3, 17] and a high contrast [49] of the physical properties (activating resonances of the highly contrasted inclusions). It has also been extended to optimize effective properties at high frequencies [37].

In this framework, a topological optimization procedure is presented in [17] to optimize dynamical properties for antiplane shear waves based on homogenization. The main ingredients are the following ones:

1. the two-scale asymptotic homogenization method is deployed,
2. a cost functional is constructed from the homogenized model,
3. its topological derivative is computed,
4. the cost functional minimization is performed thanks to a level-set algorithm,
5. the level-set is iterated by computing cell problems using FFT-accelerated solvers.

Noticeably, works on the optimization in dynamics of microstructured thin layers are more scarce and recent: [32] for an optimization of slabs based on their far-field behavior and [36] for a design of acoustic metasurfaces based on a homogenization model. In the present paper, we perform a sensitivity analysis and the optimization of an acoustic microstructured interface, based on the homogenized model of [30] and following the same overall approach as in [17]. The novelties compared to [36] and [17] are (i) the calculation of topological derivatives and their use *prior to the topological optimization process* to perform a sensitivity analysis of the effective properties and to determine valuable initializations from the closed-form formula provided by the topological derivatives for elliptical inclusions, and (ii) the use of nonconventional

FFT-based solvers to address the specific *unbounded* cell problems that arise from the two-scale homogenization of microstructured interfaces.

The paper is organized as follows. The homogenized model is recalled in section 2, and an analysis of the macroscopic observables is performed, leading to the definition of the considered optimization problem. In section 3, the topological derivatives of the effective parameters of the interface model are derived and validated numerically. Then, in section 4, based on the analytical information provided by these derivatives, a topological sensitivity-based analysis is performed for microstructures made of elliptic inclusions, and "asymptotically optimal" ellipses are determined for the chosen cost functional. Then a topological optimization scheme, which relies on the topological derivatives to update the material distribution at each iteration, is presented in section 5. We finally summarize the results and discuss possible perspectives in section 6.

2. Microstructured interfaces, effective model, and optimization problem.

2.1. Setting and homogenization. Let us consider the propagation of waves in two dimensions across a periodic row of inclusions $\cup_i \Omega_{\mathrm{i}}$ embedded within a homogeneous matrix Ω_m. The thickness and the period of the row are denoted by e and h, respectively, and we assume that $e = \mathcal{O}(h)$. The time and the spatial coordinates are denoted by t and $\boldsymbol{X} = (X_1, X_2)$, respectively, with X_2 being the direction of periodicity of the inclusions as shown in Figure 1. Antiplane elastic waves are considered, and both media are assumed to be isotropic and homogeneous. The microstructured medium is therefore characterized by two constitutive parameters, the mass density ρ_h and the shear modulus μ_h, that are piecewise constant,

$$(\rho_h, \mu_h)(\boldsymbol{X}) = \begin{cases} (\rho_{\mathrm{m}}, \mu_{\mathrm{m}}) & \text{in the matrix,} \\ (\rho_{\mathrm{i}}, \mu_{\mathrm{i}}) & \text{in the inclusions,} \end{cases} \tag{2.1}$$

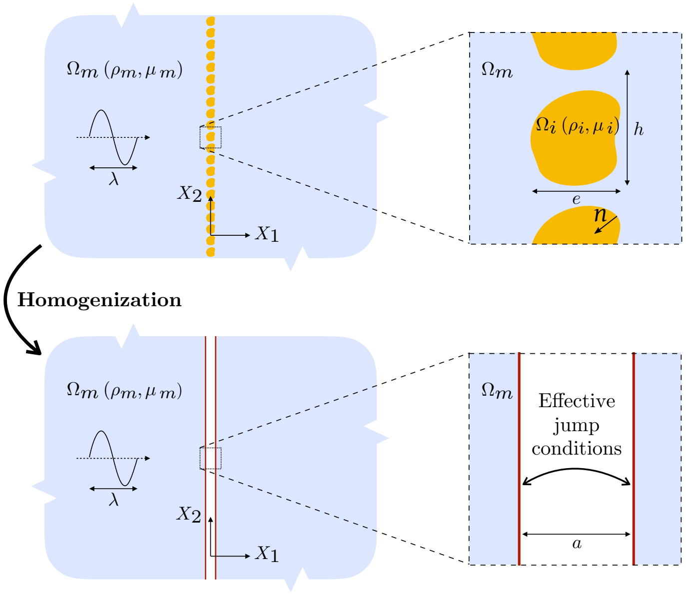

FIG. 1. *Homogenization process for a single periodic array of inclusions. Top: Original configuration with a thin microstructured layer. Bottom: Homogenized interface model.*

and the time-domain governing equation for the out-of-plane component U_h of the material displacement reads

$$\rho_h(\boldsymbol{X})\frac{\partial^2 U_h}{\partial t^2}(\boldsymbol{X},t) = \boldsymbol{\nabla}\cdot\big(\mu_h(\boldsymbol{X})\boldsymbol{\nabla} U_h(\boldsymbol{X},t)\big) + \rho_{\mathrm{m}}\delta(\boldsymbol{X}-\boldsymbol{X}_S)g(t), \tag{2.2}$$

where g is a source term located at a point $\boldsymbol{X}_S$ in the matrix. Introducing the scalar velocity field $V_h = \partial U_h/\partial t$ and the stress vector $\boldsymbol{\Sigma}_h = \mu_h \boldsymbol{\nabla} U_h$ gathering the two shear components of the stress tensor, this system can be rewritten as a first-order system in time:

$$\begin{cases} \dfrac{\partial \boldsymbol{\Sigma}_h}{\partial t}(\boldsymbol{X},t) = \mu_h(\boldsymbol{X})\boldsymbol{\nabla} V_h(\boldsymbol{X},t), \\ \rho_h(\boldsymbol{X})\dfrac{\partial V_h}{\partial t}(\boldsymbol{X},t) = \boldsymbol{\nabla}\cdot\boldsymbol{\Sigma}_h(\boldsymbol{X},t) + \rho_{\mathrm{m}}\delta(\boldsymbol{X}-\boldsymbol{X}_S)g(t), \end{cases} \tag{2.3}$$

with V_h and $\boldsymbol{\Sigma}_h\cdot\boldsymbol{n}$ being continuous at each matrix/inclusion interface $\partial\Omega_{\mathrm{i}}$, given that $\boldsymbol{n}$ is the *inward* unit normal on each $\partial\Omega_{\mathrm{i}}$.

In the following time-domain simulations, we will only consider excitations by a source point in a medium initially at rest, i.e., $V_h(\boldsymbol{X}, t=0) = 0$ and $\boldsymbol{\Sigma}_h(\boldsymbol{X}, t=0) = \boldsymbol{0}$. This choice removes the need for studying the small-scale interactions between the initial fields and the microstructure.

Remark 2.1. The system (2.3) is also relevant to model other physical phenomena, such as acoustic waves for which the fields $\boldsymbol{\Sigma}_h$, V_h, ρ_h, and $1/\mu_h$ would stand instead for the in-plane particle velocity, acoustic pressure, compressibility, and mass density, respectively.

The assumptions of the homogenization process and the results obtained in [30] are now briefly recalled.

Hypotheses of the homogenization process. Considering that the system is excited by an incident wave or external sources, the characteristic wavelength λ within the matrix is assumed to be much larger than the period h. Defining the wavenumber within the matrix as $k_{\mathrm{m}} = 2\pi/\lambda$, we introduce the parameter

$$\eta = k_{\mathrm{m}} h \tag{2.4}$$

and we assume that $\eta \ll 1$ for the configurations of interest.

Throughout this article, only the *nonresonant* case is addressed, i.e., the physical parameters of the matrix and of the inclusions are supposed to be of the same order of magnitude. For large contrasts, e.g., for very soft but dense inclusions ($\mu_{\mathrm{i}} \ll \mu_{\mathrm{m}}$ and $\rho_{\mathrm{i}} \sim \rho_{\mathrm{m}}$), the resonances of these inclusions play a key role in the transmission of waves and should be captured by specific homogenization methods; see, e.g., [42, 48] and the references therein.

These geometrical and material assumptions allow us to homogenize the microstructure in the so-called long-wavelength, nonresonant regime.

Notation. The so-called fast scale of coordinates is $\boldsymbol{y} = \boldsymbol{X}/h = (y_1, y_2)^\top$. The domain Ω is the elementary cell $\mathbb{R}\times[-1/2, 1/2]$ in $\boldsymbol{y}$-coordinates (see Figure 2) that is repeated periodically in the y_2 direction to obtain the full domain, and $(\boldsymbol{e}_1, \boldsymbol{e}_2)$ is the canonical basis of $\mathbb{R}^2$. For any function $f(x_1)$, we define the jump and the mean value around the (centered) enlarged interface of thickness a:

$$[\![f]\!]_a = f(a/2) - f(-a/2) \qquad \text{and} \qquad \langle f\rangle_a = \frac{1}{2}\big(f(a/2) + f(-a/2)\big). \tag{2.5}$$

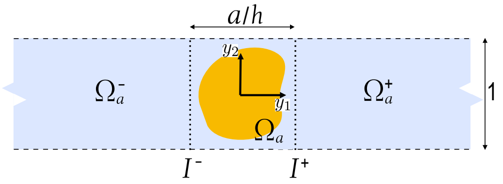

FIG. 2. *Elementary cell* Ω*, decomposed into the bounded cell* Ω^a*, and half strips* $\Omega_a^+ = [\frac{a}{2h}, +\infty[\times I^+$ *and* $\Omega_a^- =]-\infty, -\frac{a}{2h}] \times I^-$*, with* $I^\pm = \{(y_1, y_2) \in \Omega_a^\pm, \, y_1 = \pm\frac{a}{2h}\}$*.*

We will also make use of the relative material contrasts τ^μ and τ^ρ defined by

$$\tau^\mu = \frac{\mu_\mathrm{i} - \mu_\mathrm{m}}{\mu_\mathrm{m}} \quad \text{and} \quad \tau^\rho = \frac{\rho_\mathrm{i} - \rho_\mathrm{m}}{\rho_\mathrm{m}}. \tag{2.6}$$

Cell problems. The homogenization process requires the computation of auxiliary fields Φ_j for $j = 1, 2$ which are solutions of *band cell problems*. The problems initially proposed by [30] were posed on the semi-infinite representative cell Ω. For practical implementation, the authors of the present paper proposed in [18] a reformulation on a bounded rectangular cell Ω^a defined by

$$\Omega^a = \left[-\frac{a}{2h}; \frac{a}{2h}\right] \times \underbrace{\left[-\frac{1}{2}; \frac{1}{2}\right]}_{I} \tag{2.7}$$

such that the material data set

$$\boldsymbol{m}(\boldsymbol{y}) := (\rho(\boldsymbol{y}), \mu(\boldsymbol{y})) \tag{2.8}$$

satisfies

$$\boldsymbol{m}(\boldsymbol{y}) = (\rho_\mathrm{m}, \mu_\mathrm{m}) \ \forall \boldsymbol{y} \in \Omega \backslash \Omega^a, \tag{2.9}$$

as represented in Figure 2. The parameter a used in the choice of the representative cell Ω^a also defines the *effective interface width*; see Figure 1. It should satisfy $a \geq e$ to ensure that the material variations are restrained to Ω^a and for the effective model presented below to satisfy some stability conditions [30].

Using the notation $\boldsymbol{\Phi} = (\Phi_1, \Phi_2)$ for compactness, two (uncoupled) band cell problems are defined as

$$\begin{cases} \boldsymbol{\nabla} \cdot (\mu(\boldsymbol{y}) \, (\boldsymbol{\nabla\Phi} + \boldsymbol{I}_2)) = \boldsymbol{0} \text{ in } \Omega^a, \\ \boldsymbol{\Phi} \text{ is } y_2\text{-periodic}, \\ \partial_n \boldsymbol{\Phi}\left(\pm\frac{a}{2h}, \cdot\right) = \boldsymbol{\Lambda}\left(\boldsymbol{\Phi}\left(\pm\frac{a}{2h}, \cdot\right)\right) \text{ on } I^\pm, \end{cases} \tag{2.10}$$

where $\boldsymbol{I}_2$ is the second-order identity tensor, (I^-, I^+) are the left and right boundaries of Ω^a (see Figure 2), and $\boldsymbol{\Lambda}$ is a nonlocal *Dirichlet-to-Neumann* (DtN) operator; see [26, 15, 18] and the expression recalled in Appendix A for completeness. In (2.10) and hereafter, the adopted convention for the gradient components is such that $(\boldsymbol{\nabla\Phi})_{ij} = \partial\Phi_j / \partial y_i$.

These elementary solutions will serve to compute the effective parameters that appear in the homogenized model presented now.

Homogenized model. From [30], we know that the homogenization of the problem (2.3) at order $\mathcal{O}(\eta)$ in such a configuration yields the following homogenized model for the first-order approximation $(V, \boldsymbol{\Sigma})$ of $(V_h, \boldsymbol{\Sigma}_h)$:

$$\tag{2.11} \begin{cases} \dfrac{\partial \boldsymbol{\Sigma}}{\partial t}(\boldsymbol{X},t) = \mu_{\mathrm{m}} \boldsymbol{\nabla} V(\boldsymbol{X},t) & (|X_1| \geq a/2,\ X_2 \in \mathbb{R}),\\ \rho_{\mathrm{m}} \dfrac{\partial V}{\partial t}(\boldsymbol{X},t) = \boldsymbol{\nabla}\cdot\boldsymbol{\Sigma}(\boldsymbol{X},t) + \rho_{\mathrm{m}}\delta(\boldsymbol{X}-\boldsymbol{X}_S)g(t) & (|X_1| \geq a/2,\ X_2 \in \mathbb{R}),\\ [\![V]\!]_a = h\left\{\mathcal{B}\left\langle \dfrac{\partial V}{\partial X_1}\right\rangle_a + \mathcal{B}_2\left\langle \dfrac{\partial V}{\partial X_2}\right\rangle_a\right\} & (X_2 \in \mathbb{R}),\\ [\![\Sigma_1]\!]_a = h\left\{\mathcal{S}\left\langle \boldsymbol{\nabla}\cdot\boldsymbol{\Sigma}\right\rangle_a - \mathcal{C}_1\left\langle \dfrac{\partial \Sigma_1}{\partial X_2}\right\rangle_a - \mathcal{C}\left\langle \dfrac{\partial \Sigma_2}{\partial X_2}\right\rangle_a\right\} & (X_2 \in \mathbb{R}), \end{cases}$$

featuring imperfect transmission conditions for the velocity V and normal component of the stress vector $\Sigma_1 = \boldsymbol{\Sigma}\cdot\boldsymbol{e}_1$. This system will be studied both in the time domain, where the same source point and null initial conditions as in the microstructured problem will be used, and in the frequency domain for an established harmonic incident plane wave; see section 2.2 below.

The *effective coefficients* entering the transmission conditions are the parameter

$$\tag{2.12} \mathcal{S} = \frac{a}{h} + \tau^{\rho}|\Omega_{\mathrm{i}}|,$$

where $|\Omega_{\mathrm{i}}| = \int_{\Omega_{\mathrm{i}}} \mathrm{d}\boldsymbol{y}$ is the surface of the inclusion phase in the rescaled coordinates, and the four coefficients $(\mathcal{B}, \mathcal{B}_2, \mathcal{C}_1, \mathcal{C})$, with the notation of [30]. They are gathered in the two vector-valued parameters $\boldsymbol{\mathcal{B}} = (\mathcal{B}, \mathcal{B}_2)$ and $\boldsymbol{\mathcal{C}} = (\mathcal{C}_1, \mathcal{C})$ and are expressed in terms of the elementary solution $\boldsymbol{\Phi}$ to (2.10) as

$$\tag{2.13} \boldsymbol{\mathcal{B}}(\boldsymbol{m}) = \frac{a}{h}\boldsymbol{e}_1 + \int_I \left[\boldsymbol{\Phi}\left(\frac{a}{2h}, y_2\right) - \boldsymbol{\Phi}\left(-\frac{a}{2h}, y_2\right)\right] \mathrm{d}y_2$$

and

$$\tag{2.14} \boldsymbol{\mathcal{C}}(\boldsymbol{m}) = \int_{\Omega^a} \frac{\mu(\boldsymbol{y})}{\mu_{\mathrm{m}}} \left(\frac{\partial \boldsymbol{\Phi}}{\partial y_2}(\boldsymbol{y}) + \boldsymbol{e}_2\right) \mathrm{d}\boldsymbol{y}.$$

Important properties of the coefficients $(\mathcal{B}_2, \mathcal{C}_1)$ were also proven in [30], namely

- $\mathcal{B}_2 = -\mathcal{C}_1$ in all cases,
- $\mathcal{B}_2 = \mathcal{C}_1 = 0$ for the cells that are symmetric with respect to the medium horizontal plane $y_2 = 0$; see Figure 2 (e.g., for circular inclusions).

Finally, the interface energy associated with the homogenized problem (2.11) is proven to be positive as soon as a is greater than e [30], ensuring stability of the solution to (2.11). In the harmonic regime, the well-posedness of similar homogenized models with effective jump conditions has been tackled in [21, 22]. Instabilities in the time-domain for a system associated to a negative interface energy were analyzed and illustrated in [23].

Hereafter, the effective parameters are collected in $\boldsymbol{m}_{\mathrm{eff}}$ as

$$\tag{2.15} \boldsymbol{m}_{\mathrm{eff}} := (\mathcal{B}, \mathcal{B}_2, \mathcal{S}, \mathcal{C}_1, \mathcal{C}).$$

2.2. Analysis of macroscopic observables and optimization problem. In this section, the aim is to identify macroscopic effects specific to the microstructured interfaces, described by the homogenized model in the considered long-wavelength regime. To find an optimal design that would enhance these effects, an optimization problem should be established. To do so, we use some analytical macroscopic observables of the homogenized problem, which are the scattering coefficients computed for incident plane waves in the time-harmonic regime, together with observations from time-domain simulations with point sources. The considered optimization problem is finally given.

2.2.1. Scattering coefficients for time-harmonic plane waves. In this section, we consider an established time-harmonic regime at circular frequency ω. We therefore use the frequency-domain formulation of the homogenized model (2.11) with $g=0$, which is equivalent to the model obtained by applying homogenization in the frequency domain; see [48]. Introducing the amplitude of the time-harmonic wavefield $\hat{\boldsymbol{\mathcal{U}}}(\boldsymbol{X},\omega)=(\hat{V}(\boldsymbol{X},\omega),\hat{\Sigma}_1(\boldsymbol{X},\omega),\hat{\Sigma}_2(\boldsymbol{X},\omega))^{\mathrm{T}}$ and its decomposition $\hat{\boldsymbol{\mathcal{U}}}=\hat{\boldsymbol{\mathcal{U}}}_{\mathrm{I}}+\hat{\boldsymbol{\mathcal{U}}}_{\mathrm{R}}+\hat{\boldsymbol{\mathcal{U}}}_{\mathrm{T}}$ into incident $\hat{\boldsymbol{\mathcal{U}}}_{\mathrm{I}}$, reflected $\hat{\boldsymbol{\mathcal{U}}}_{\mathrm{R}}$, and transmitted $\hat{\boldsymbol{\mathcal{U}}}_{\mathrm{T}}$ waves, we consider incident *plane* waves given by

$$\hat{\boldsymbol{\mathcal{U}}}_{\mathrm{I}}(\boldsymbol{X},\omega)=\begin{pmatrix} 1/\mu_m \\ -\cos\theta_{\mathrm{I}}/c_{\mathrm{m}} \\ -\sin\theta_{\mathrm{I}}/c_{\mathrm{m}} \end{pmatrix}\exp(-\mathrm{i}\boldsymbol{k}_{\mathrm{I}}\cdot\boldsymbol{X}) \tag{2.16}$$

with $c_{\mathrm{m}}=\sqrt{\mu_{\mathrm{m}}/\rho_{\mathrm{m}}}$ the celerity of waves in the matrix, θ_{I} the direction of propagation, and $\boldsymbol{k}_{\mathrm{I}}=(\omega/c_{\mathrm{m}})(\cos(\theta_{\mathrm{I}}),\sin(\theta_{\mathrm{I}}))$ the corresponding wavevector.

We also look for reflected and transmitted plane waves as

$$\begin{cases} \hat{\boldsymbol{\mathcal{U}}}_{\mathrm{R}}(\boldsymbol{X},\omega)=\begin{pmatrix} 1/\mu_m \\ -\cos\theta_{\mathrm{R}}/c_{\mathrm{m}} \\ -\sin\theta_{\mathrm{R}}/c_{\mathrm{m}} \end{pmatrix}\exp(-\mathrm{i}\boldsymbol{k}_{\mathrm{R}}\cdot\boldsymbol{X})\,\mathcal{R}(\theta_{\mathrm{I}},\omega), \\ \hat{\boldsymbol{\mathcal{U}}}_{\mathrm{T}}(\boldsymbol{X},\omega)=\begin{pmatrix} 1/\mu_m \\ -\cos\theta_{\mathrm{T}}/c_{\mathrm{m}} \\ -\sin\theta_{\mathrm{T}}/c_{\mathrm{m}} \end{pmatrix}\exp(-\mathrm{i}\boldsymbol{k}_{\mathrm{T}}\cdot\boldsymbol{X})\,\mathcal{T}(\theta_{\mathrm{I}},\omega). \end{cases} \tag{2.17}$$

Inserting the expression above in the frequency-domain jump conditions (see [47]), the reflection and transmission angles are classically found to be $\theta_{\mathrm{R}}=\pi-\theta_{\mathrm{I}}$ and $\theta_{\mathrm{T}}=\theta_{\mathrm{I}}$ ($\boldsymbol{k}_{\mathrm{R}}$ and $\boldsymbol{k}_{\mathrm{T}}$ are the corresponding wavevectors with the same wavenumber ω/c_{m}), and the expression of the reflection and transmission coefficients $\mathcal{R}$ and $\mathcal{T}$ can be obtained analytically. They read, respectively,

$$\begin{cases} \mathcal{R}(\theta_{\mathrm{I}},\omega)=\dfrac{\mathrm{i}\omega\,\mathscr{L}}{\mathscr{Z}+\mathrm{i}\omega\,\mathscr{N}-\omega^2\mathscr{M}}\exp\left(\mathrm{i}\dfrac{\omega}{c_{\mathrm{m}}}a\cos\theta_{\mathrm{I}}\right), \\ \mathcal{T}(\theta_{\mathrm{I}},\omega)=\dfrac{\mathscr{Z}+\mathrm{i}\omega\,\mathscr{G}+\omega^2\mathscr{M}}{\mathscr{Z}+\mathrm{i}\omega\,\mathscr{N}-\omega^2\mathscr{M}}\exp\left(\mathrm{i}\dfrac{\omega}{c_{\mathrm{m}}}a\cos\theta_{\mathrm{I}}\right), \end{cases} \tag{2.18}$$

with $c_{\mathrm{m}}=\sqrt{\mu_m/\rho_{\mathrm{m}}}$ and

$$\begin{cases} \mathscr{L}=h\left(\mathcal{B}\cos(\theta_{\mathrm{I}})^2+\mathcal{C}\sin(\theta_{\mathrm{I}})^2-\mathcal{S}\right), \\ \mathscr{Z}=2c_{\mathrm{m}}\cos\theta_{\mathrm{I}}, \\ \mathscr{N}=h\left(-\mathcal{C}\sin(\theta_{\mathrm{I}})^2+\mathcal{B}\cos(\theta_{\mathrm{I}})^2+\mathcal{S}\right), \\ \mathscr{M}=\dfrac{h^2}{2c_{\mathrm{m}}}\left(\mathcal{B}_2\mathcal{C}_1\sin(\theta_{\mathrm{I}})^2-\mathcal{B}\mathcal{C}\sin(\theta_{\mathrm{I}})^2+\mathcal{B}\mathcal{S}\right)\cos(\theta_{\mathrm{I}}), \\ \mathscr{G}=-h(-\mathcal{C}_1+\mathcal{B}_2)\cos(\theta_{\mathrm{I}})\sin(\theta_{\mathrm{I}}). \end{cases} \tag{2.19}$$

One can notice a symmetry with respect to the change $\theta_\mathrm{I} \to -\theta_\mathrm{I}$ for the reflection coefficient $\mathcal{R}(\theta_\mathrm{I}, \omega)$ and for the modulus of the transmission coefficient $|\mathcal{T}(\theta_\mathrm{I}, \omega)|$. Consequently, only the argument of the transmission coefficient $\arg(\mathcal{T}(\theta_\mathrm{I}, \omega))$ is not symmetric with respect to the normal incidence. The quantity $\mathscr{G}$ defined in (2.19) and proportional to $\mathcal{B}_2 = -\mathcal{C}_1$ is responsible for this asymmetry, which is therefore obtained for cells that are nonsymmetric with respect to the horizontal plane $y_2 = 0$.

From this observation, we chose to focus on these nonsymmetric geometries, to exhibit and enhance macroscopic effects that would not appear for symmetric configurations more studied in the literature (say, circular or rectangular inclusions aligned with the main axes [30]).

2.2.2. Observations from time-domain simulations. To investigate these configurations, one considers a microstructure typical of steel in concrete, for which the physical parameters are given by Table 1. The periodicity length is $h = 1$m and the examples of two geometries for the inclusion Ω_i are investigated: one ellipse of semiaxes lengths (0.15, 0.5) tilted of $-\pi/4$ and one rectangle of sizes (1.25, 0.08) tilted of $-\pi/4$. The effective parameters associated to these two configurations are computed and time-domain simulations are performed in the associated effective media in a rectangular domain $\boldsymbol{X} \in [-70; 35] \times [-132; 132]$.

In this part, the considered excitation is no longer an incident plane wave but a source point $\delta(\boldsymbol{X} - \boldsymbol{X}_\mathrm{S}) g(t)$, with $g(t)$ a sufficiently regular, wide-band signal. Here we choose g defined as

$$g(t) = \begin{cases} A \displaystyle\sum_{m=1}^{4} \alpha_m \sin(\beta_m \, \omega_c \, t) & \text{if } 0 < t < \dfrac{1}{f_c}, \\ 0 \text{ otherwise,} \end{cases} \tag{2.20}$$

where $\beta_m = 2^{m-1}$ and the coefficients α_m being $\alpha_1 = 1$, $\alpha_2 = -21/32$, $\alpha_3 = 63/768$, $\alpha_4 = -1/512$. It entails that $g \in C^6([0, +\infty[)$ and $g(t)$ is a wide-band signal with a central frequency $f_c = \omega_c / 2\pi$. The source is located at $\boldsymbol{X}_\mathrm{S} = (-35, 0)$, with $X_1 = 0$ being the center of the enlarged effective interface. The central frequency is $f_c = 50$ Hz, which corresponds to a small parameter $\eta = 0.14$ for which a good agreement between the homogenized model and the microstructured configuration has been observed. The time-domain simulations are performed thanks to finite differences and to the explicit simplified interface method [28] to handle the effective enlarged interface.

To highlight the interface contribution, we define and compute the incident fields $\boldsymbol{\mathcal{U}}_\mathrm{I}$ as the fields which would propagate in the matrix only (without interface) for this excitation, and introduce the *scattered* fields $\boldsymbol{\mathcal{U}}_\mathbf{sc} = (V_\mathrm{sc}, (\boldsymbol{\Sigma}_\mathrm{sc})_1, (\boldsymbol{\Sigma}_\mathrm{sc})_2)^\mathrm{T} = \boldsymbol{\mathcal{U}} - \boldsymbol{\mathcal{U}}_\mathrm{I}$, which are computed from time $t = 0$ until $t_\mathrm{f} = 86.7$ ms. From these data, one can compute the local cumulative energy defined as

$$\mathcal{E}(\boldsymbol{X}) = \frac{1}{2} \int_0^{t_\mathrm{f}} \left(\frac{1}{\mu_\mathrm{m}} \boldsymbol{\Sigma}_\mathrm{sc}(\boldsymbol{X}, t)^2 + \rho_\mathrm{m} V_\mathrm{sc}(\boldsymbol{X}, t)^2 \right) \mathrm{d}t. \tag{2.21}$$

This quantity is evaluated on the right of the interface for both microstructures in Figures 3(a) and 3(b) as a function of the polar coordinates (r, θ) centered at $\boldsymbol{X}_\mathrm{S}$,

TABLE 1
Physical parameters considered for the microstructure.

μ_i	ρ_i	μ_m	ρ_m
78 GPa	7800 $\mathrm{kg} \cdot \mathrm{m}^{-3}$	12 GPa	2500 $\mathrm{kg} \cdot \mathrm{m}^{-3}$

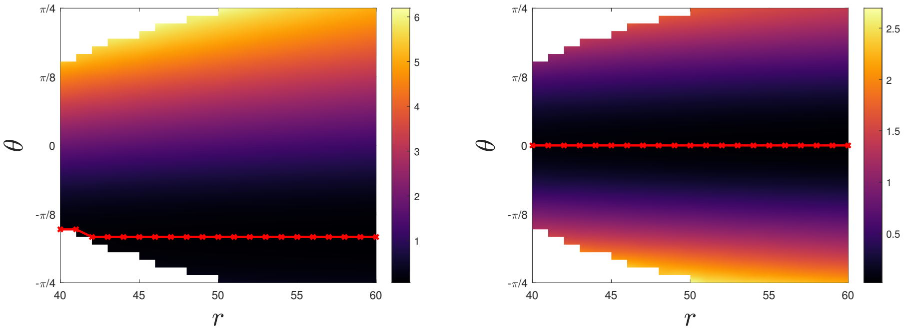

(a) $\mathcal{E}(r,\theta)$ for elliptic inclusions (b) $\mathcal{E}(r,\theta)$ for rectangular inclusions

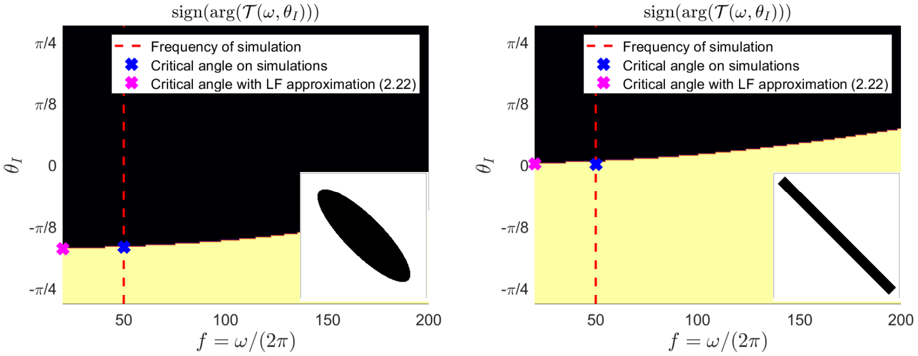

(c) sign(arg($\mathcal{T}$)) for elliptic inclusions (d) sign(arg($\mathcal{T}$)) for rectangular inclusions

FIG. 3. *Cumulative energy in polar coordinates (first row) where the position of the minimal value for a given r is denoted by the red crosses, and study of sign(*arg*($\mathcal{T}$)) (second row, yellow and black for positive and negative signs, respectively), computed with the effective model corresponding to elliptic (left) and rectangular (right) inclusions. (Color online.)*

with $r \in [40; 60]$. For each value of r, we observe that the energy $\mathcal{E}$ is minimal for a given angle $\theta_{\min}$, denoted by red crosses. Moreover, one can notice that this value $\theta_{\min}$ seems to be independant of r. Furthermore, the sign of $\arg(\mathcal{T})$ is plotted in Figures 3(c) and 3(d) (black and yellow maps where yellow and black stand for positive and negative signs, respectively) for the same two microstructures directly using the analytical formula (2.19), as a function of θ_{I} and ω. It is then observed that this critical value measured on time-domain simulations (denoted by the blue cross) seems to coincide with the value of θ_{I} for which $\arg(\mathcal{T})$ changes sign at low frequency.

These observations suggest a link between the two characterizations of microstructured interfaces presented above, namely (i) the effective scattering coefficients computed from the homogenized model and (ii) the angle $\theta_{\min}$ of minimal scattered energy, measured numerically for a circular incident wave. Considering that minimizing the energy emitted by a known source, in a chosen direction $\theta_{\min}$, is a problem of interest for, e.g., directive sound attenuation, we therefore aim at designing microstructures associated with a vanishing $\arg(\mathcal{T}(\theta_{\mathrm{I}}, \omega))$ for $\theta_{\mathrm{I}} = \theta_{\min}$ and low frequencies.

2.2.3. Optimization problem. To exhibit an analytical link between the critical value $\theta_{\min}$ at low frequency and the homogenized coefficients $\boldsymbol{m}_{\text{eff}}$, one considers a first-order approximation for the transmission coefficient $\mathcal{T}$. In this low-frequency limit, we consider a fixed geometry and therefore a fixed value of h, while ω, and consequently η, tends to 0. Upon introducing $\bar{\mathscr{G}} = \mathscr{G}/h$, $\bar{\mathscr{M}} = 2c_{\rm m}\mathscr{M}/h^2$, and $\bar{\mathscr{N}} = \mathscr{N}/h$ in (2.18) and (2.19), this leads to

$$\begin{aligned}\mathcal{T}(\theta_{\rm I},\omega) &= \frac{\mathscr{Z} + {\rm i}\eta c_{\rm m}\bar{\mathscr{G}} + \eta^2\frac{c_{\rm m}}{2}\bar{\mathscr{M}}}{\mathscr{Z} + {\rm i}\eta c_{\rm m}\bar{\mathscr{N}} - \eta^2\frac{c_{\rm m}}{2}\bar{\mathscr{M}}}\exp\left({\rm i}\eta\frac{a}{h}\cos(\theta_{\rm I})\right)\\ &= \frac{1 + {\rm i}\eta\frac{\bar{\mathscr{G}}}{2\cos(\theta_{\rm I})} + \mathcal{O}(\eta^2)}{1 + {\rm i}\eta\frac{\bar{\mathscr{N}}}{2\cos(\theta_{\rm I})} + \mathcal{O}(\eta^2)}\left(1 + {\rm i}\eta\frac{a}{h}\cos(\theta_{\rm I}) + \mathcal{O}(\eta^2)\right)\\ &= 1 + {\rm i}\eta\left(\frac{\bar{\mathscr{G}} - \bar{\mathscr{N}}}{2\cos(\theta_{\rm I})} + \frac{a}{h}\cos(\theta_{\rm I})\right) + \mathcal{O}(\eta^2).\end{aligned} \tag{2.22}$$

This can be summarized as

$$\mathcal{T}(\theta_{\rm I},\omega) = 1 + {\rm i}\eta\,\mathcal{T}_1(\boldsymbol{m}_{\rm eff},\theta_{\rm I}) + \mathcal{O}(\eta^2) \tag{2.23}$$

with $\mathcal{T}_1(\boldsymbol{m}_{\rm eff},\theta_{\rm I})$ given by

$$\begin{aligned}\mathcal{T}_1(\boldsymbol{m}_{\rm eff},\theta_{\rm I}) &= -\mathcal{B}_2\sin(\theta_{\rm I}) + \frac{\mathcal{C}\sin(\theta_{\rm I})^2 - \mathcal{B}\cos(\theta_{\rm I})^2 - \mathcal{S}}{2\cos(\theta_{\rm I})} + \frac{a}{h}\cos(\theta_{\rm I})\\ &= -\mathcal{B}_2\sin(\theta_{\rm I}) + \frac{\mathcal{C}^\star\sin(\theta_{\rm I})^2 - \mathcal{B}^\star\cos(\theta_{\rm I})^2 - \mathcal{S}^\star}{2\cos\theta_{\rm I}},\end{aligned} \tag{2.24}$$

where

$$\mathcal{B}^\star = \mathcal{B} - a/h, \quad \mathcal{C}^\star = \mathcal{C} - a/h, \quad \text{and} \quad \mathcal{S}^\star = \mathcal{S} - a/h = \tau^\rho|\Omega_{\rm i}|. \tag{2.25}$$

The second expression in (2.24), using the coefficients in (2.25), shows that $\mathcal{T}_1$ does not depend on the choice of the interface thickness a and will be used in section 4 to slightly simplify the computations.

With the approximation (2.23), it is clear that, at low frequency, $\arg(\mathcal{T})$ changes sign when $\mathcal{T}_1(\boldsymbol{m}_{\rm eff},\theta_{\rm I})$ changes sign. This is confirmed in Figures 3(c) and 3(d), where the angle for which $\mathcal{T}_1$ changes signs is denoted by a pink cross and is observed to be very close to both the critical angle observed in numerical simulations and the angle for which the exact value of $\arg(\mathcal{T})$ changes signs at low frequency.

Canceling the function $\mathcal{T}_1$ then seems to be a good way to reach the aforementioned effect. Moreover, we will aim at simultaneously maximizing the derivative amplitude $|\partial_\theta\mathcal{T}_1|$ with

$$\partial_\theta\mathcal{T}_1 = \frac{\partial\mathcal{T}_1}{\partial\theta_{\rm I}} \tag{2.26}$$

to (i) avoid close-to-zero local minima of $|\mathcal{T}_1|$ without sign change and (ii) "push" the ensuing optimization process toward "stiff" sign changes. For a given critical angle $\theta_{\rm min}$, these two objectives will be addressed in two ways:

1. In section 4, asymptotic closed-form formulas of $\mathcal{T}_1$ and $\partial_\theta\mathcal{T}_1$ obtained for small elliptic inclusions will be used to obtain "asymptotically optimal" ellipses.
2. In section 5, a topological optimization algorithm will be proposed to find an optimal material distribution $\boldsymbol{m}_{\rm opt}$ in the bounded cell Ω^a that satisfies the following optimization problem:

$$\begin{aligned}&\text{Find} \qquad \arg\min_{\boldsymbol{m}}\tilde{\mathcal{J}}_{\rm main}(\boldsymbol{m})\\ &\text{with} \qquad \tilde{\mathcal{J}}_{\rm main}(\boldsymbol{m}) = \mathcal{J}_{\rm main}(\boldsymbol{m}_{\rm eff}) = \left(\frac{\mathcal{T}_1(\boldsymbol{m}_{\rm eff},\theta_{\rm min})}{\partial_\theta\mathcal{T}_1(\boldsymbol{m}_{\rm eff},\theta_{\rm min})}\right)^2.\end{aligned} \tag{2.27}$$

> In particular, ellipses obtained in the previous step will be used as initializations. Additional terms will be added to the functional $\mathcal{J}_{\text{main}}$ in (2.27) in order to reach a given surface ratio between the materials, or to have a sufficient smoothness of the final configuration. The resulting total cost functional $\mathcal{J}$ will be introduced in section 5.

In both cases, we will rely on the computation of the topological derivatives of the effective coefficients performed in section 3 below.

Remark 2.2. Although the focus is on controlling transmitted energy and on the related functional (2.27) in this paper, the topological derivatives calculated in section 3 and the optimization methods described in section 5 could be used for any other objective.

3. Topological derivatives of the effective parameters.

In this section, one aims at describing the sensitivity of the effective parameters to periodic topological changes of the microstructure, i.e., geometric perturbations of the representative cell Ω^a. A perturbation is defined as a small inhomogeneity $\mathcal{P}_{\boldsymbol{z},\varepsilon} = \boldsymbol{z} + \varepsilon\mathcal{P}$ of size ε, normalized shape $\mathcal{P}$, and physical parameters $(\mu + \Delta\mu, \rho + \Delta\rho)$ introduced at a point $\boldsymbol{z} \in \Omega^a$. The material perturbation is $\Delta\boldsymbol{m} = (\Delta\rho, \Delta\mu)$ with $\Delta\mu > -\min_{\boldsymbol{y}\in\Omega^a} \mu(\boldsymbol{y})$ and $\Delta\rho > -\min_{\boldsymbol{y}\in\Omega^a} \rho(\boldsymbol{y})$ to satisfy the physical positivity constraints. The resulting perturbed cell, denoted by $\Omega^a_{\boldsymbol{z},\varepsilon}$ and represented in Figure 4, features the physical parameters

$$\boldsymbol{m}_{\boldsymbol{z},\varepsilon} := (\mu_{\boldsymbol{z},\varepsilon}, \rho_{\boldsymbol{z},\varepsilon}) = (\mu + \Delta\mu\chi_{\mathcal{P}_{\boldsymbol{z},\varepsilon}}, \rho + \Delta\rho\chi_{\mathcal{P}_{\boldsymbol{z},\varepsilon}}) \tag{3.1}$$

with $\chi_{\mathcal{P}_{\boldsymbol{z},\varepsilon}}$ the characteristic function of the perturbation domain $\mathcal{P}_{\boldsymbol{z},\varepsilon}$.

Remark 3.1. The definition of $\Delta\boldsymbol{m}$ may depend on the choice of $\boldsymbol{z}$ if the unperturbed cell is heterogeneous. However, we disregard the case where the perturbation is located at an interface between two different materials. Consequently, we will drop any dependence of $\Delta\boldsymbol{m}$ on the space coordinate in the notation, since they do not change the integrals computed hereafter. Moreover, the computation of the topological derivatives is performed for an arbitrary material perturbation $\Delta\boldsymbol{m}$, as represented in Figure 4. However, in numerical examples we will only consider phase swapping.

Let f be a function of the material properties. In this two-dimensional context, the so-called topological derivative of the function f, denoted by $\mathcal{D}f$, is defined thanks to the following two-dimensional asymptotic expansion:

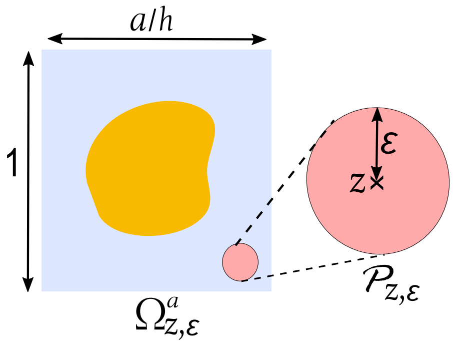

FIG. 4. *Cell $\Omega^a_{\boldsymbol{z},\varepsilon}$ perturbed by the introduction of the inhomogeneity $\mathcal{P}_{\boldsymbol{z},\varepsilon}$.*

$$f_{\boldsymbol{z},\varepsilon} := f(\boldsymbol{m}_{\boldsymbol{z},\varepsilon}) \underset{\varepsilon\to 0}{=} f(\boldsymbol{m}) + \varepsilon^2 \mathcal{D}f(\boldsymbol{m},\boldsymbol{z},\mathcal{P},\Delta\boldsymbol{m}) + o(\varepsilon^2). \tag{3.2}$$

It describes the influence on the function f of a perturbation located at $\boldsymbol{z}$, of shape $\mathcal{P}$ and material perturbation $\Delta\boldsymbol{m}$. Therefore, the more negative $\mathcal{D}f(\boldsymbol{m},\boldsymbol{z},\mathcal{P},\Delta\boldsymbol{m})$ is, the more efficient such a perturbation at point $\boldsymbol{z}$ would be to decrease f.

In this section, the topological derivatives of the effective parameters collected in (2.15) are computed. First, one looks for an expansion of the solution $\boldsymbol{\Phi}_{\boldsymbol{z},\varepsilon}$ to the cell problem (2.10) in the perturbed cell Ω^a_ε in section 3.1. This allows the computation of the topological sensitivities of the five effective parameters in section 3.2.

3.1. Approximation of the perturbed cell problem solution. To compute the topological derivatives of the homogenized coefficients, we must characterize the asymptotic behavior of the cell function $\boldsymbol{\Phi}$ in (2.10) when the topological perturbation (3.1) is introduced. To this end, we first reformulate the cell problem (2.10) into an integral equation, more suitable for the asymptotic analysis. This analysis is then pursued formally, i.e., rigorous remainder estimates are not provided. However, such estimates are given by [14, Proposition 5], and we expect similar arguments to hold given the similarity between the present cell problem and the one addressed in [14].

Weak forms of the unperturbed and perturbed cell problems. The first step is to write the weak form of the cell problem. To do so, we consider a function $v \in H^1_{\mathrm{per}} = \{u \in H^1(\Omega^a;\mathbb{R}),\ u\ y_2\text{-periodic}\}$. The first equation of (2.10) is then multiplied by v and integrated by parts in Ω^a. Using the periodicity condition and the boundary conditions in (2.10), one obtains after a division by μ_{m}

$$\boldsymbol{\mathcal{A}}_\mu(\boldsymbol{\Phi}, v) = -\boldsymbol{F}_\mu(v) + \boldsymbol{J}(v) \qquad \forall v \in H^1_{\mathrm{per}}, \tag{3.3}$$

where one has introduced the following functionals for $\boldsymbol{u} = (u_1, u_2) \in H^1_{\mathrm{per}} \times H^1_{\mathrm{per}}$ and $v \in H^1_{\mathrm{per}}$:

$$\begin{cases} \boldsymbol{\mathcal{A}}_\mu(\boldsymbol{u}, v) = \displaystyle\int_{\Omega^a} \frac{\mu(\boldsymbol{y})}{\mu_{\mathrm{m}}} \boldsymbol{\nabla}\boldsymbol{u}(\boldsymbol{y})^\top \cdot \boldsymbol{\nabla} v(\boldsymbol{y})\mathrm{d}\boldsymbol{y} + \mathcal{L}^-(\boldsymbol{u}, v) + \mathcal{L}^+(\boldsymbol{u}, v), \\ \boldsymbol{F}_\mu(v) = \displaystyle\int_{\Omega^a} \frac{\mu(\boldsymbol{y})}{\mu_{\mathrm{m}}} \boldsymbol{\nabla} v(\boldsymbol{y})\mathrm{d}\boldsymbol{y}, \\ \boldsymbol{J}(v) = \displaystyle\int_I \left[v\left(\frac{a}{2h}, y_2\right) - v\left(-\frac{a}{2h}, y_2\right) \right] \boldsymbol{e}_1 \mathrm{d}y_2 \end{cases} \tag{3.4}$$

with

$$\mathcal{L}^\pm(\boldsymbol{u}, v) = -\int_I \boldsymbol{\Lambda} \left[\boldsymbol{u}\left(\pm\frac{a}{2h}, \cdot\right) \right](y_2)\, v\left(\pm\frac{a}{2h}, y_2\right) \mathrm{d}y_2. \tag{3.5}$$

The vector-valued weak formulation (3.3), involving a scalar-valued test function, reflects the two uncoupled problems satisfied by the components (Φ_1, Φ_2).

Similarly, the perturbed field $\boldsymbol{\Phi}_{\boldsymbol{z},\varepsilon}$ satisfies for all $v \in H^1(\Omega^a;\mathbb{R})$, v y_2-periodic

$$\boldsymbol{\mathcal{A}}_{\mu_{\boldsymbol{z},\varepsilon}}(\boldsymbol{\Phi}_{\boldsymbol{z},\varepsilon}, v) = -\boldsymbol{F}_\mu(v) - \boldsymbol{\delta F}_{\boldsymbol{z},\varepsilon}(v) + \boldsymbol{J}(v) \tag{3.6}$$

with

$$\boldsymbol{\delta F}_{\boldsymbol{z},\varepsilon}(v) = \frac{\Delta\mu}{\mu_{\mathrm{m}}} \int_{\mathcal{P}_{\boldsymbol{z},\varepsilon}} \boldsymbol{\nabla} v(\boldsymbol{y})\mathrm{d}\boldsymbol{y}. \tag{3.7}$$

Integral equation. To obtain the integral equation satisfied by $\boldsymbol{\Phi}_{\boldsymbol{z},\varepsilon}$, one then introduces the Green's function $G(\cdot,\boldsymbol{x})$ associated with a point source at $\boldsymbol{x}\in\Omega^a$, i.e., the solution of

$$\begin{cases} -\boldsymbol{\nabla}_{\boldsymbol{y}}\cdot\left(\dfrac{\mu(\boldsymbol{y})}{\mu_{\mathrm{m}}}\boldsymbol{\nabla}_{\boldsymbol{y}}G(\boldsymbol{y},\boldsymbol{x})\right)=\delta(\boldsymbol{y}-\boldsymbol{x}) \quad \forall\boldsymbol{y}\in\Omega^a, \\ G(\cdot,\boldsymbol{x})\ y_2\text{-periodic}, \\ -\boldsymbol{n}\cdot\boldsymbol{\nabla}_{\boldsymbol{y}}G(\boldsymbol{y},\boldsymbol{x})\Big|_{y_1=\pm\frac{a}{2h}}=\Lambda\left[G(\boldsymbol{y},\boldsymbol{x})\right]\Big|_{y_1=\pm\frac{a}{2h}} \quad \forall\boldsymbol{y}\in I^{\pm}. \end{cases} \tag{3.8}$$

It can be decomposed as

$$G(\boldsymbol{y},\boldsymbol{x})=G_\infty\left(\boldsymbol{y}-\boldsymbol{x};\frac{\mu(\boldsymbol{x})}{\mu_{\mathrm{m}}}\right)+G_c(\boldsymbol{y},\boldsymbol{x}), \quad \text{with} \quad G_\infty(\boldsymbol{r};\mu_\star)=-\frac{\ln(\|\boldsymbol{r}\|)}{2\pi\mu_\star}, \tag{3.9}$$

where G_∞ is the full-space Green's function solution of the two-dimensional Poisson equation that shares the same singularity as G, and G_c is the complementary part to the Green's function solution accounting for the heterogeneity of the cell and the boundary conditions. Details about these functions are given in Appendix B.

For any sufficiently smooth function $\boldsymbol{w}$, one gets from (3.8) the integral representation for all $\boldsymbol{x}\in\Omega^a$:

$$\boldsymbol{w}(\boldsymbol{x})=\boldsymbol{\mathcal{A}}_\mu(\boldsymbol{w},G(\cdot,\boldsymbol{x})) \tag{3.10}$$

with $\boldsymbol{\mathcal{A}}_\mu$ defined in (3.4).

Coming back to the perturbed problem, one introduces the surface integral operator $\boldsymbol{\mathcal{N}}_{\boldsymbol{z},\varepsilon}$:

$$\boldsymbol{\mathcal{N}}_{\boldsymbol{z},\varepsilon}\boldsymbol{f}(\boldsymbol{x})=\frac{\Delta\mu}{\mu_{\mathrm{m}}}\int_{\mathcal{P}_{\boldsymbol{z},\varepsilon}}\boldsymbol{\nabla}\boldsymbol{f}(\boldsymbol{y})^\top\cdot\boldsymbol{\nabla}_{\boldsymbol{y}}G(\boldsymbol{y},\boldsymbol{x})\mathrm{d}\boldsymbol{y}. \tag{3.11}$$

The choice of piecewise-regular material properties μ ensures the regularity of $\boldsymbol{\Phi}$ away from inner interfaces, which in turn allows us to use $\boldsymbol{w}=\boldsymbol{\Phi}$ in the integral representation (3.10). We can, in addition, set $v=G(\cdot,\boldsymbol{x})$ in the weak form (3.6) (the resulting integral being defined although $G(\cdot,\boldsymbol{x})$ does not belong to $H^1(\Omega^a,\mathbb{R})$). Together with the definition (3.4) of $\boldsymbol{\mathcal{A}}_\mu$ one obtains

$$\begin{aligned} \boldsymbol{\mathcal{A}}_\mu(\boldsymbol{\Phi}_{\boldsymbol{z},\varepsilon},G(\cdot,\boldsymbol{x}))+\boldsymbol{\mathcal{N}}_{\boldsymbol{z},\varepsilon}\boldsymbol{\Phi}_{\boldsymbol{z},\varepsilon}(\boldsymbol{x}) &= -\boldsymbol{F}_\mu(G(\cdot,\boldsymbol{x}))-\boldsymbol{\delta F}_{\boldsymbol{z},\varepsilon}(G(\cdot,\boldsymbol{x}))+\boldsymbol{J}(G(\cdot,\boldsymbol{x})) \\ &= \boldsymbol{\mathcal{A}}_\mu(\boldsymbol{\Phi},G(\cdot,\boldsymbol{x}))-\boldsymbol{\delta F}_{\boldsymbol{z},\varepsilon}(G(\cdot,\boldsymbol{x})), \end{aligned} \tag{3.12}$$

where in the last line we used $v=G(\cdot,\boldsymbol{x})$ in (3.3). Finally, one considers $\boldsymbol{w}=\boldsymbol{\Phi}_{\boldsymbol{z},\varepsilon}$ and $\boldsymbol{w}=\boldsymbol{\Phi}$ in (3.10). Together with (3.12) this leads to the integral equation satisfied by the perturbed field $\boldsymbol{\Phi}_{\boldsymbol{z},\varepsilon}$:

$$(\boldsymbol{I}+\boldsymbol{\mathcal{N}}_{\boldsymbol{z},\varepsilon})(\boldsymbol{\Phi}_{\boldsymbol{z},\varepsilon})(\boldsymbol{x})=\boldsymbol{\Phi}(\boldsymbol{x})-\boldsymbol{\delta F}_{\boldsymbol{z},\varepsilon}(G(\cdot,\boldsymbol{x})), \tag{3.13}$$

where the integral operator $\boldsymbol{\mathcal{N}}_{\boldsymbol{z},\varepsilon}$ and right-hand-side term $\boldsymbol{\delta F}_{\boldsymbol{z},\varepsilon}(G(\cdot,\boldsymbol{x}))$ are both supported by the perturbation domain $\mathcal{P}_{\boldsymbol{z},\varepsilon}$.

Asymptotic analysis. Aiming at reformulating (3.13) onto the reference shape $\mathcal{P}$, let us introduce the scaled coordinates $\boldsymbol{x}=\boldsymbol{z}+\varepsilon\bar{\boldsymbol{x}}$ and assume the following expansion, based on previous work [14], for all $\boldsymbol{x}\in\mathcal{P}_{\boldsymbol{z},\varepsilon}$:

$$\boldsymbol{\Phi}_{\boldsymbol{z},\varepsilon}(\boldsymbol{x})=\boldsymbol{\Phi}(\boldsymbol{z})+\varepsilon\boldsymbol{\Phi}_1(\bar{\boldsymbol{x}})+o(\varepsilon). \tag{3.14}$$

One also writes the following Taylor expansion for the cell function:

$$\boldsymbol{\Phi}(\boldsymbol{x})=\boldsymbol{\Phi}(\boldsymbol{z})+\varepsilon\bar{\boldsymbol{x}}\cdot\boldsymbol{\nabla}\boldsymbol{\Phi}(\boldsymbol{z})+o(\varepsilon). \tag{3.15}$$

Inserting (3.14) and (3.15) in (3.13) and keeping only the leading and first-order terms yield

$$(\boldsymbol{I}+\boldsymbol{\mathcal{N}}_{\boldsymbol{z},\varepsilon})\left(\varepsilon\boldsymbol{\Phi}_1\left(\frac{\cdot-\boldsymbol{z}}{\varepsilon}\right)\right)(\boldsymbol{x})=\varepsilon\bar{\boldsymbol{x}}\cdot\boldsymbol{\nabla}\boldsymbol{\Phi}(\boldsymbol{z})-\boldsymbol{\delta F}_{\boldsymbol{z},\varepsilon}(G(\cdot,\boldsymbol{x})), \tag{3.16}$$

since $\boldsymbol{\mathcal{N}}_{\boldsymbol{z},\varepsilon}\boldsymbol{\Phi}(\boldsymbol{z})=\boldsymbol{0}$. As developed in Appendix B, $\boldsymbol{\nabla}G_\infty$ is homogeneous of degree -1 (see (B.1)) and $\boldsymbol{\nabla}G_c(\cdot,\boldsymbol{x})$ is regular in the neighborhood of $\boldsymbol{z}$ (see (B.5)). The function G in (3.8) then satisfies

$$\boldsymbol{\nabla}_{\boldsymbol{y}}G(\boldsymbol{y},\boldsymbol{x})=\varepsilon^{-1}\boldsymbol{\nabla}G_\infty\left(\bar{\boldsymbol{y}}-\bar{\boldsymbol{x}};\frac{\mu(\boldsymbol{z})}{\mu_{\mathrm{m}}}\right)+o(\varepsilon^{-1}). \tag{3.17}$$

Inserting the above expansion in (3.16), performing a change of variables to rewrite the integral on $\mathcal{P}$, and identifying the leading-order ($O(\varepsilon)$) contributions then leads to the scaled integral equation:

$$(\boldsymbol{I}+\boldsymbol{\mathcal{M}})(\widetilde{\boldsymbol{\Phi}}_1)(\bar{\boldsymbol{x}})=\bar{\boldsymbol{x}}\cdot(\boldsymbol{\nabla}\boldsymbol{\Phi}(\boldsymbol{z})+\boldsymbol{I}) \tag{3.18}$$

with $\widetilde{\boldsymbol{\Phi}}_1(\bar{\boldsymbol{x}})=\boldsymbol{\Phi}_1(\bar{\boldsymbol{x}})+\bar{\boldsymbol{x}}$ and $\boldsymbol{\mathcal{M}}$ defined by

$$\boldsymbol{\mathcal{M}}\boldsymbol{f}(\bar{\boldsymbol{x}})=\frac{\Delta\mu}{\mu_{\mathrm{m}}}\int_{\mathcal{P}}\boldsymbol{\nabla}\boldsymbol{f}(\bar{\boldsymbol{y}})^{\top}\cdot\boldsymbol{\nabla}G_\infty\left(\bar{\boldsymbol{y}}-\bar{\boldsymbol{x}};\frac{\mu(\boldsymbol{z})}{\mu_{\mathrm{m}}}\right)\mathrm{d}\bar{\boldsymbol{y}}. \tag{3.19}$$

Consequently, introducing $\boldsymbol{R}$, the vector solution of the equation

$$(\boldsymbol{I}+\boldsymbol{\mathcal{M}})\boldsymbol{R}(\bar{\boldsymbol{x}})=\bar{\boldsymbol{x}}, \tag{3.20}$$

i.e., the solution to a free-space transmission problem associated with a perturbation $(\mathcal{P},\Delta\mu)$, with a homogeneous background of modulus $\mu(\boldsymbol{z})$, then $\widetilde{\boldsymbol{\Phi}}_1$ is given by

$$\widetilde{\boldsymbol{\Phi}}_1(\bar{\boldsymbol{x}})=\boldsymbol{R}(\bar{\boldsymbol{x}})\cdot(\boldsymbol{\nabla}\boldsymbol{\Phi}(\boldsymbol{z})+\boldsymbol{I}). \tag{3.21}$$

Finally, one inserts this in (3.14) to get the first-order expansion:

$$\boldsymbol{\Phi}_{\boldsymbol{z},\varepsilon}(\boldsymbol{x})=\boldsymbol{\Phi}(\boldsymbol{z})+\varepsilon\left(\boldsymbol{R}(\bar{\boldsymbol{x}})\cdot(\boldsymbol{\nabla}\boldsymbol{\Phi}(\boldsymbol{z})+\boldsymbol{I})-\bar{\boldsymbol{x}}\right)+o(\varepsilon). \tag{3.22}$$

3.2. Calculation of the topological derivatives.

The results of this section are summarized in the following proposition.

PROPOSITION 3.2. *The topological derivatives of the effective coefficients* $\mathcal{S},\boldsymbol{\mathcal{B}},\boldsymbol{\mathcal{C}}$*, for a material perturbation* $(\Delta\mu,\Delta\rho)$ *supported by the domain* $\mathcal{P}_{\boldsymbol{z},\varepsilon}=\boldsymbol{z}+\varepsilon\mathcal{P}$*, are given by*

$$\mathcal{D}\mathcal{S}(\boldsymbol{m},\boldsymbol{z},\mathcal{P},\Delta\boldsymbol{m})=\frac{\Delta\rho}{\rho_{\mathrm{m}}}|\mathcal{P}|, \tag{3.23}$$

$$\boldsymbol{\mathcal{D}\mathcal{B}}(\boldsymbol{m},\boldsymbol{z},\mathcal{P},\Delta\boldsymbol{m})=-(\boldsymbol{\nabla}\Phi_1(\boldsymbol{z})+\boldsymbol{e}_1)\cdot\boldsymbol{A}(\mathcal{P},\mu(\boldsymbol{z}),\Delta\mu)\cdot(\boldsymbol{\nabla\Phi}(\boldsymbol{z})+\boldsymbol{I}), \tag{3.24}$$

$$\boldsymbol{\mathcal{D}\mathcal{C}}(\boldsymbol{m},\boldsymbol{z},\mathcal{P},\Delta\boldsymbol{m})=(\boldsymbol{\nabla}\Phi_2(\boldsymbol{z})+\boldsymbol{e}_2)\cdot\boldsymbol{A}(\mathcal{P},\mu(\boldsymbol{z}),\Delta\mu)\cdot(\boldsymbol{\nabla\Phi}(\boldsymbol{z})+\boldsymbol{I}), \tag{3.25}$$

where the so-called polarization tensor $\boldsymbol{A}$ *is defined from the solution* $\boldsymbol{R}$ *of the problem* (3.20) *as*

$$\boldsymbol{A}(\mathcal{P},\mu(\boldsymbol{z}),\Delta\mu)=\frac{\Delta\mu}{\mu_{\mathrm{m}}}\int_{\mathcal{P}}\boldsymbol{\nabla}_{\bar{\boldsymbol{y}}}\boldsymbol{R}(\bar{\boldsymbol{y}})\mathrm{d}\bar{\boldsymbol{y}}. \tag{3.26}$$

Remark 3.3. The polarization tensor $\boldsymbol{A}$ has been used in previous studies [16, 4, 14], where it is sometimes derived using layer potentials rather than volume (surface in two dimensions) integral operators (resulting in possibly different prefactors). It is also related to the concentration (or localization) tensor $\mathbb{A}=\int_{\mathcal{P}}\boldsymbol{\nabla}_{\bar{\boldsymbol{y}}}\boldsymbol{R}(\bar{\boldsymbol{y}})\mathrm{d}\bar{\boldsymbol{y}}$ much used in micromechanics [40]. It is symmetric and is known analytically for a variety of inclusion shapes $\mathcal{P}$; see [40]. In particular, for an elliptic perturbation of semiaxes lengths $(1,\gamma)$ along directions $(\boldsymbol{a}_1,\boldsymbol{a}_2)$, it is given by

$$\boldsymbol{A}(\mathcal{P},\mu(\boldsymbol{z}),\Delta\mu)=\pi\gamma(\gamma+1)\frac{\Delta\mu}{\mu_{\mathrm{m}}}\left(\frac{\boldsymbol{a}_1\otimes\boldsymbol{a}_1}{1+\gamma+\gamma\frac{\Delta\mu}{\mu(\boldsymbol{z})}}+\frac{\boldsymbol{a}_2\otimes\boldsymbol{a}_2}{1+\gamma+\frac{\Delta\mu}{\mu(\boldsymbol{z})}}\right). \tag{3.27}$$

Remark 3.4. The topological derivative of a functional f most often involves a *direct field* (here $\boldsymbol{x}+\boldsymbol{\Phi}$) and an *adjoint field* depending on f; see, e.g., [7, 38]. In the present case, the adjoint fields corresponding to coefficients $\boldsymbol{\mathcal{B}}$ and $\boldsymbol{\mathcal{C}}$ would be found to be $-(x_1+\Phi_1)$ and $x_2+\Phi_2$, respectively, as seen in the formula of Proposition 3.2, established in a more direct way below.

The steps of the proof of Proposition 3.2 are now given.

3.2.1. Computation of $\boldsymbol{\mathcal{D}\mathcal{S}}$.

We first notice that, owing to the definition of $\mathcal{S}$ in (2.12), one has

$$\mathcal{S}(\boldsymbol{m})=\int_{\Omega^a}\frac{\rho(\boldsymbol{y})}{\rho_{\mathrm{m}}}\mathrm{d}\boldsymbol{y}. \tag{3.28}$$

Consequently, one gets

$$\mathcal{S}_{\boldsymbol{z},\varepsilon}=\mathcal{S}(\boldsymbol{m})+\int_{\mathcal{P}_{\boldsymbol{z},\varepsilon}}\frac{\Delta\rho}{\rho_{\mathrm{m}}}\mathrm{d}\boldsymbol{y}=\mathcal{S}(\boldsymbol{m})+\varepsilon^2\frac{\Delta\rho}{\rho_{\mathrm{m}}}|\mathcal{P}|, \tag{3.29}$$

which yields by identification with (3.2) the following result:

$$\mathcal{D}\mathcal{S}(\boldsymbol{m},\boldsymbol{z},\mathcal{P},\Delta\boldsymbol{m})=\frac{\Delta\rho}{\rho_{\mathrm{m}}}|\mathcal{P}|. \tag{3.30}$$

3.2.2. Computation of $\boldsymbol{\mathcal{D}\mathcal{B}}$.

From the expression (2.13), the effective parameter $\boldsymbol{\mathcal{B}}_{\boldsymbol{z},\varepsilon}$ associated with the perturbed cell reads

$$\boldsymbol{\mathcal{B}}_{\boldsymbol{z},\varepsilon}=\boldsymbol{\mathcal{B}}(\boldsymbol{m})+\int_I\left[\boldsymbol{\delta\Phi}_{\boldsymbol{z},\varepsilon}\left(\frac{a}{2h},y_2\right)-\boldsymbol{\delta\Phi}_{\boldsymbol{z},\varepsilon}\left(-\frac{a}{2h},y_2\right)\right]\mathrm{d}y_2, \tag{3.31}$$

with the pertubation for the solution of the cell problem $\boldsymbol{\delta\Phi}_{\boldsymbol{z},\varepsilon}$ defined by

$$\boldsymbol{\delta\Phi}_{\boldsymbol{z},\varepsilon} = \boldsymbol{\Phi}_{\boldsymbol{z},\varepsilon} - \boldsymbol{\Phi}. \tag{3.32}$$

The left-hand side of (3.6) reads

$$\boldsymbol{\mathcal{A}}_{\mu_{\boldsymbol{z},\varepsilon}}(\boldsymbol{\Phi}_{\boldsymbol{z},\varepsilon}, v) = \boldsymbol{\mathcal{A}}_{\mu}(\boldsymbol{\Phi}, v) + \boldsymbol{\mathcal{A}}_{\mu}(\boldsymbol{\delta\Phi}_{\boldsymbol{z},\varepsilon}, v) + \frac{\Delta\mu}{\mu_{\mathrm{m}}}\int_{\mathcal{P}_{\boldsymbol{z},\varepsilon}} \boldsymbol{\nabla\Phi}_{\boldsymbol{z},\boldsymbol{\varepsilon}}(\boldsymbol{y})^{\top} \cdot \boldsymbol{\nabla} v(\boldsymbol{y})\mathrm{d}\boldsymbol{y}. \tag{3.33}$$

Inserting this equation in (3.6) and using (3.3), one gets for all $v \in H^1_{\mathrm{per}}$

$$\boldsymbol{\mathcal{A}}_{\mu}(\boldsymbol{\delta\Phi}_{\boldsymbol{z},\varepsilon}, v) + \frac{\Delta\mu}{\mu_{\mathrm{m}}}\int_{\mathcal{P}_{\boldsymbol{z},\varepsilon}} \boldsymbol{\nabla\Phi}_{\boldsymbol{z},\boldsymbol{\varepsilon}}(\boldsymbol{y})^{\top} \cdot \boldsymbol{\nabla} v(\boldsymbol{y})\mathrm{d}\boldsymbol{y} = -\boldsymbol{\delta F}_{\boldsymbol{z},\varepsilon}(v). \tag{3.34}$$

Furthermore, $\beta = \Phi_1 + y_1$ satisfies for all $\boldsymbol{w} \in H^1(\Omega^a;\mathbb{R}^2)$, $\boldsymbol{w}$ y_2-periodic

$$\boldsymbol{\mathcal{A}}_{\mu}(\boldsymbol{w}, \beta) = \int_I \left[\boldsymbol{w}\left(\frac{a}{2h}, y_2\right) - \boldsymbol{w}\left(-\frac{a}{2h}, y_2\right)\right] \mathrm{d}y_2. \tag{3.35}$$

Taking $v = \beta$ in (3.34) and $\boldsymbol{w} = \boldsymbol{\delta\Phi}_{\boldsymbol{z},\varepsilon}$ in (3.35), the expansion (3.31) reads

$$\boldsymbol{\mathcal{B}}_{\boldsymbol{z},\varepsilon} = \boldsymbol{\mathcal{B}}(\boldsymbol{m}) - \frac{\Delta\mu}{\mu_{\mathrm{m}}}\int_{\mathcal{P}_{\boldsymbol{z},\varepsilon}} \boldsymbol{\nabla}\beta(\boldsymbol{y}) \cdot (\boldsymbol{\nabla\Phi}_{\boldsymbol{z},\varepsilon}(\boldsymbol{y}) + \boldsymbol{I})\mathrm{d}\boldsymbol{y}. \tag{3.36}$$

Consequently, one looks for an asymptotic expansion for $\boldsymbol{\nabla\Phi}_{\boldsymbol{z},\varepsilon}$. For this purpose, one uses the final expansion (3.22) of the previous section. One also writes the expansion $\boldsymbol{\nabla}\beta(\boldsymbol{y}) = \boldsymbol{\nabla}\beta(\boldsymbol{z}) + o(1)$ for all $\boldsymbol{y} \in \mathcal{P}_{\boldsymbol{z},\varepsilon}$ and expresses the integral in the scaled coordinates as

$$\boldsymbol{\mathcal{B}}_{\boldsymbol{z},\varepsilon} = \boldsymbol{\mathcal{B}}(\boldsymbol{m}) - \frac{\Delta\mu}{\mu_{\mathrm{m}}}\int_{\mathcal{P}} \boldsymbol{\nabla}\beta(\boldsymbol{z}) \cdot \left(\frac{1}{\varepsilon}\boldsymbol{\nabla\Phi}_{\boldsymbol{z},\varepsilon}(\bar{\boldsymbol{y}}) + \boldsymbol{I}\right)\varepsilon^2\mathrm{d}\bar{\boldsymbol{y}} + o(\varepsilon^2). \tag{3.37}$$

Inserting the expansion (3.22) in the above equation yields

$$\boldsymbol{\mathcal{B}}_{\boldsymbol{z},\varepsilon} = \boldsymbol{\mathcal{B}}(\boldsymbol{m}) - \varepsilon^2\frac{\Delta\mu}{\mu_{\mathrm{m}}}\boldsymbol{\nabla}\beta(\boldsymbol{z}) \cdot \int_{\mathcal{P}} \boldsymbol{\nabla R}(\bar{\boldsymbol{y}})\mathrm{d}\bar{\boldsymbol{y}} \cdot (\boldsymbol{\nabla\Phi}(\boldsymbol{z}) + \boldsymbol{I}) + o(\varepsilon^2). \tag{3.38}$$

Using the definition $\beta = \Phi_1 + y_1$ and the polarization tensor $\boldsymbol{A}$ defined by (3.26), the topological derivative of $\boldsymbol{\mathcal{B}}$ reads

$$\boldsymbol{\mathcal{DB}}(\boldsymbol{m}, \boldsymbol{z}, \mathcal{P}, \Delta\boldsymbol{m}) = -(\boldsymbol{\nabla}\Phi_1(\boldsymbol{z}) + \boldsymbol{e}_1) \cdot \boldsymbol{A}(\mathcal{P}, \mu(\boldsymbol{z}), \Delta\mu) \cdot (\boldsymbol{\nabla\Phi}(\boldsymbol{z}) + \boldsymbol{I}). \tag{3.39}$$

3.2.3. Computation of $\boldsymbol{\mathcal{DC}}$.

From the expression (2.14), the effective parameter $\boldsymbol{\mathcal{C}}_{\boldsymbol{z},\varepsilon}$ associated with the perturbed cell reads

$$\boldsymbol{\mathcal{C}}_{\boldsymbol{z},\varepsilon} = \boldsymbol{\mathcal{C}}(\boldsymbol{m}) + \int_{\Omega^a} \frac{\mu(\boldsymbol{y})}{\mu_{\mathrm{m}}}\frac{\partial\boldsymbol{\delta\Phi}_{\boldsymbol{z},\varepsilon}}{\partial y_2}(\boldsymbol{y})\mathrm{d}\boldsymbol{y} + \frac{\Delta\mu}{\mu_{\mathrm{m}}}\int_{\mathcal{P}_{\boldsymbol{z},\varepsilon}} \left(\frac{\partial\boldsymbol{\Phi}_{\boldsymbol{z},\varepsilon}}{\partial y_2}(\boldsymbol{y}) + \boldsymbol{e}_2\right)\mathrm{d}\boldsymbol{y} + o(\varepsilon^2). \tag{3.40}$$

We know that Φ_2 satisfies for all $\boldsymbol{w} \in H^1_{\mathrm{per}}$

$$\boldsymbol{\mathcal{A}}_{\mu}(\boldsymbol{w}, \Phi_2) = -\int_{\Omega^a} \frac{\mu(\boldsymbol{y})}{\mu_{\mathrm{m}}}\frac{\partial\boldsymbol{w}}{\partial y_2}(\boldsymbol{y})\mathrm{d}\boldsymbol{y}. \tag{3.41}$$

One takes $v = \Phi_2$ in (3.34) and $\boldsymbol{w} = \boldsymbol{\delta\Phi}_{\boldsymbol{z},\varepsilon}$ in (3.41) and gets

$$\int_{\Omega^a} \frac{\mu(\boldsymbol{y})}{\mu_\mathrm{m}} \frac{\partial \boldsymbol{\delta\Phi}_{\boldsymbol{z},\varepsilon}}{\partial y_2}(\boldsymbol{y})\mathrm{d}\boldsymbol{y} = \frac{\Delta\mu}{\mu_\mathrm{m}} \int_{\mathcal{P}_{\boldsymbol{z},\varepsilon}} \boldsymbol{\nabla}\Phi_2(\boldsymbol{y}) \cdot (\boldsymbol{\nabla\Phi}_{\boldsymbol{z},\varepsilon}(\boldsymbol{y}) + \boldsymbol{I})\mathrm{d}\boldsymbol{y}, \tag{3.42}$$

which yields

$$\boldsymbol{\mathcal{C}}_{\boldsymbol{z},\varepsilon} = \boldsymbol{\mathcal{C}}(\boldsymbol{m}) + \frac{\Delta\mu}{\mu_\mathrm{m}} \int_{\mathcal{P}_{\boldsymbol{z},\varepsilon}} (\boldsymbol{\nabla}\Phi_2(\boldsymbol{y}) + \boldsymbol{e}_2) \cdot (\boldsymbol{\nabla\Phi}_{\boldsymbol{z},\varepsilon}(\boldsymbol{y}) + \boldsymbol{I})\mathrm{d}\boldsymbol{y} + o(\varepsilon^2). \tag{3.43}$$

Once again, we use the Taylor expansion $\boldsymbol{\nabla}\Phi_2(\boldsymbol{y}) = \boldsymbol{\nabla}\Phi_2(\boldsymbol{z}) + o(1)$ for all $\boldsymbol{y}$ in $\mathcal{P}_{\boldsymbol{z},\varepsilon}$, the expression of the integral in the scaled coordinates, and the expansion (3.22) to get the final expression for the topological derivative,

$$\boldsymbol{\mathcal{DC}}(\boldsymbol{m}, \boldsymbol{z}, \mathcal{P}, \Delta\boldsymbol{m}) = (\boldsymbol{\nabla}\Phi_2(\boldsymbol{z}) + \boldsymbol{e}_2) \cdot \boldsymbol{A}(\mathcal{P}, \mu(\boldsymbol{z}), \Delta\mu) \cdot (\boldsymbol{\nabla\Phi}(\boldsymbol{z}) + \boldsymbol{I}). \tag{3.44}$$

3.3. Numerical validation. To validate numerically the found expressions of the topological derivatives, we can compute the errors made by the approximation of $\boldsymbol{\mathcal{B}}_{\boldsymbol{z},\varepsilon}$ and $\boldsymbol{\mathcal{C}}_{\boldsymbol{z},\varepsilon}$ by $\boldsymbol{\mathcal{B}} + \varepsilon^2\boldsymbol{\mathcal{DB}}$ and $\boldsymbol{\mathcal{C}} + \varepsilon^2\boldsymbol{\mathcal{DC}}$, respectively. Indeed, due to (3.38) and (3.43), these errors should be of order ε^3 at least.

One starts with an initial reference configuration ($\varepsilon = 0$), then computes numerically the solutions of the cell problems (2.10) (their computation will be briefly described in section 5.1.1), and thus the values of $\boldsymbol{\mathcal{B}}$ and $\boldsymbol{\mathcal{C}}$ from (2.13) and (2.14). The initial configuration is chosen to be heterogeneous in order to avoid simplifications than can occur with a homogeneous medium as reference. More precisely, we choose a homogeneous medium containing an elliptic inclusion of center $(0,0)$ and semiaxes lengths $(0.32\,\mathrm{m},\ 0.1\,\mathrm{m})$, tilted of 45°. The physical parameters are again given in Table 1. Then one inserts a perturbation in the background matrix at $\boldsymbol{z} = (-0.26\ \mathrm{m}, 0.24\ \mathrm{m})$. Its physical parameters are the ones of the elliptic inclusion $(\rho_\mathrm{i}, \mu_\mathrm{i})$. Its shape is an ellipse of semiaxes lengths $(\varepsilon,\ 0.6\,\varepsilon)$ and tilted of 45°. For $\varepsilon = 0.1$, the configuration is plotted in Figure 5(b). For a given value of ε, one computes the perturbed cell solutions and thus the exact effective parameters $\boldsymbol{\mathcal{B}}_{\boldsymbol{z},\varepsilon}$ and $\boldsymbol{\mathcal{C}}_{\boldsymbol{z},\varepsilon}$ from (2.13) and (2.14). Their first-order approximations $\boldsymbol{\mathcal{B}} + \varepsilon^2\boldsymbol{\mathcal{DB}}$ and $\boldsymbol{\mathcal{C}} + \varepsilon^2\boldsymbol{\mathcal{DC}}$ are computed from (3.24) and (3.25) using (3.27).

The relative errors between the exact and approximated values, for instance, $|(\mathcal{B}_1)_{\boldsymbol{z},\varepsilon} - \mathcal{B}_1 - \varepsilon^2\mathcal{DB}_1|/|(\mathcal{B}_1)_{\boldsymbol{z},\varepsilon}|$, are plotted as functions of the perturbation size ε

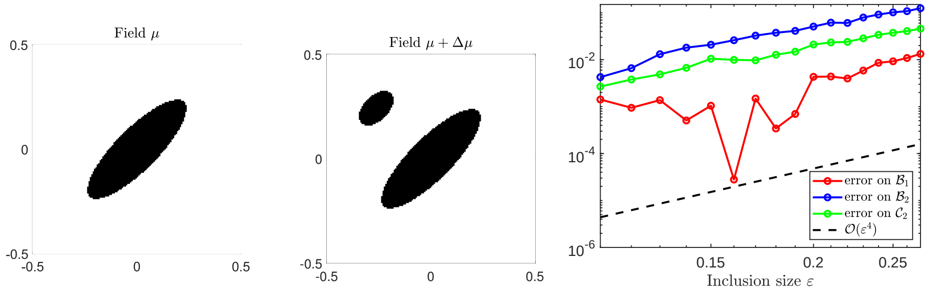

(a) Reference Ω^a (b) Perturbed cell $\Omega^a_{\boldsymbol{z},\varepsilon}$ (c)

FIG. 5. *Test case for an elliptic perturbation.* (a) *Reference configuration.* (b) *Perturbed configuration for $\varepsilon = 0.1$.* (c) *Relative errors between the exact and approximated effective parameters as functions of ε in a log-log scale.*

in log-log scale in Figure 5(c). Since $\mathcal{B}_2 = \mathcal{C}_1$, only one of the corresponding misfits is represented. The dashed line stands for an error of $\mathcal{O}(\varepsilon^4)$. It seems that this is the actual order of approximation of the effective parameters, the small variations for low values of ε being probably due to numerical errors in the computation of the coefficients. This underlines the fact that the leading-order terms and consequently the topological derivatives are well accounted for and that the terms of order ε^3 in the expansions (3.38) and (3.43) are probably equal to zero for this type of perturbation with a central symmetry. This was already observed for volume microstructures in [13, 14], with the intuition that it occurs for perturbations with a central symmetry. This remains, however, to be proved. In the case where there is not any central symmetry, we therefore expect an error of order $\mathcal{O}(\varepsilon^3)$.

4. Approximate parametric optimization in the case of elliptic inclusions. In this section, the topological derivatives are used as tools to analyze the case of cells made of a unique *elliptic* inclusion Ω_i in a homogeneous material. First, the quality of the approximation of the effective parameters in this case is investigated. Then, we show that "asymptotically optimal" ellipses can be determined with respect to the optimization problem presented in section 2.2.

4.1. Approximation of the effective parameters. Consider a unique inclusion in an otherwise homogeneous cell, a configuration which can be seen as a single perturbation in a homogeneous reference cell. In this case, the effective coefficient $\mathcal{S}^\star = \mathcal{S} - a/h$ in (2.25) is given by the exact expression,

$$\mathcal{S}^\star = \varepsilon^2 |\mathcal{P}| \tau^\rho, \tag{4.1}$$

while the topological derivatives formula provides the following approximations:

$$\mathcal{B}^\star = -\varepsilon^2 A_{11} + o(\varepsilon^2), \quad \mathcal{B}_2 = -\varepsilon^2 A_{12} + o(\varepsilon^2), \quad \mathcal{C}^\star = \varepsilon^2 A_{22} + o(\varepsilon^2), \tag{4.2}$$

where $\mathcal{S}^\star$, $\mathcal{B}^\star$, and $\mathcal{C}^\star$ are defined in (2.25).

Computing these approximations only requires the knowledge of the polarization tensor (3.27) for the perturbation shape $\mathcal{P}$, and the scaling of the result by ε^2. This is much less costly than computing numerically the cell solutions and the associated effective parameters for each choice of inclusion, especially for elliptic inclusions for which the polarization tensor is known analytically.

As an example of the quality of these approximations, we consider an ellipse, located at $\boldsymbol{z} = (0, 0)$, of tilted angle $\varphi = 40°$, and semiaxes lengths $(\varepsilon,\ 0.2\,\varepsilon)$. In Figure 6(b), the relative errors between the numerically computed value of the effective parameters through (2.13)–(2.14) and their approximations given above are represented for an increasing value of ε. In this case, the reference values themselves decay in $\mathcal{O}(\varepsilon^2)$ as the single inclusion in the cell vanishes. The relative error (e.g., $|(\mathcal{B}^\star)_{\boldsymbol{z},\varepsilon} + \varepsilon^2 A_{11}|/|(\mathcal{B}^\star)_{\boldsymbol{z},\varepsilon}|$), i.e., the ratio between the residual (supposedly in $\mathcal{O}(\varepsilon^4)$ for ellipses) and this reference value, is therefore expected to be in $\mathcal{O}(\varepsilon^2)$, which is observed in the figure. We also observe that a good agreement is obtained even for high values of ε (i.e., even outside the asymptotic regime). Indeed, for $\varepsilon = 0.5$ (illustrated in Figure 6(a)) the major axis length is equal to the size of the unit cell and the relative errors remain below 15%.

Remark 4.1. The approximation (4.2), using only the polarization tensor computed from the free-space transmission problem (3.20), is well-known in the domain of micromechanics as the "dilute" or "Eshelby" approximation (see, for instance, [40]

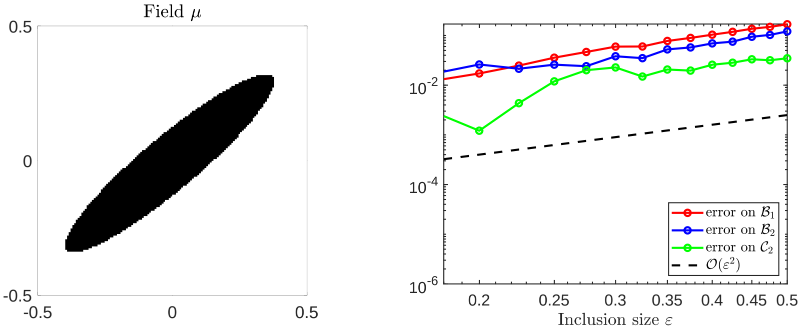

(a) (b)

FIG. 6. *Test case for an elliptic inclusion.* (a) *Configuration for* $\varepsilon = 0.5$. (b) *Relative errors between the exact and approximated effective parameters as functions of inclusion size* ε *in a log-log scale.*

and the numerous references therein). It does not account for interactions between inclusions, and is therefore supposedly restricted to very low concentrations of inclusions, but provides surprisingly accurate results in the present context.

Consequently, we propose to use the expressions (4.2) to obtain "optimal" ellipses that solve the optimization problem presented in section 2.2.

4.2. Normal incidence: Explicit formula and analysis. When the case of interest is normal incidence of waves, i.e., when $\theta_{\mathrm{I}} = 0$, closed-form results are available, that are used in this section as a first example. Indeed, the expression (2.23) of the function of interest $\mathcal{T}_1$ is considerably simplified, as

$$\mathcal{T}_1(\theta_{\mathrm{I}} = 0) = -\frac{1}{2}(\mathcal{B}^\star + \mathcal{S}^\star) = -\frac{\varepsilon^2}{2}(-A_{11} + \pi\gamma\tau^\rho) + o(\varepsilon^2). \tag{4.3}$$

Then, pairs of tilted angle and aspect ratio (φ, γ) for which $\mathcal{T}_1 = o(\varepsilon^2)$ can be found analytically for given material contrasts (τ^ρ, τ^μ). Indeed, canceling the leading-order term above and introducing the expression (3.27) of the polarization tensor gives

$$\pi\gamma\tau^\rho = A_{11} \Leftrightarrow \quad \tau^\rho = (1+\gamma)\tau^\mu\left(\frac{\cos^2(\varphi)}{1+\gamma+\gamma\tau^\mu} + \frac{\sin^2(\varphi)}{1+\gamma+\tau^\mu}\right), \tag{4.4}$$

which leads to

$$\tau^\rho(1+\gamma+\gamma\tau^\mu)(1+\gamma+\tau^\mu) - \tau^\mu(1+\gamma)^2 - (\tau^\mu)^2(1+\gamma)(\gamma + (1-\gamma)\cos^2(\varphi)) = 0. \tag{4.5}$$

Therefore, we eventually get

$$\begin{cases} \varphi = \arccos\sqrt{\beta} & \text{if } \beta \geq 0, \\ \quad \text{no solution} & \text{if } \beta < 0, \end{cases} \quad \text{with } \beta = \frac{[\tau^\rho(1+\gamma+\tau^\mu) - \tau^\mu(1+\gamma)]\,(1+\gamma+\gamma\tau^\mu)}{(\tau^\mu)^2(1-\gamma^2)}. \tag{4.6}$$

This particular solution can be used to check the numerical implementation of $\mathcal{T}_1$.

As discussed in section 2.2.3, to find an optimal pair $(\varphi^{\mathrm{opt}}, \gamma^{\mathrm{opt}})$, we also aim at maximizing the absolute value of the derivative, $|\partial_\theta \mathcal{T}_1(\theta_{\mathrm{I}} = 0)|$ along the curve defined by the function (4.6) above. To do so, we rely again on the simplified expression of the function $\partial_\theta \mathcal{T}_1$ for normal incidence ($\theta_{\mathrm{I}} = 0$) and on the approximations (4.2) of the effective coefficients, and use the approximation

$$\begin{aligned}\partial_\theta \mathcal{T}_1(\theta_{\mathrm{I}} = 0) &= -\mathcal{B}_2 = \varepsilon^2 A_{12} + o(\varepsilon^2) \\ &= \frac{\varepsilon^2 \sin(2\varphi)}{2} \frac{\pi\gamma(1-\gamma^2)(\tau^\mu)^2}{[1+\gamma(1+\tau^\mu)][1+\gamma+\tau^\mu]} + o(\varepsilon^2).\end{aligned} \tag{4.7}$$

Then plugging the expression (4.6) of φ, one obtains an expression for the leading-order contribution of $\partial_\theta \mathcal{T}_1$ as a function of γ only, whose maximum is easily found numerically, as represented in Figure 7.

Finally, we compute the numerical "true" values of the functions $\mathcal{T}_1$ and $\partial_\theta \mathcal{T}_1$ and the cost functional $\mathcal{J}_{\mathrm{main}}$ defined by (2.27), used here as a quality indicator of a given geometry. For nonvanishing inclusions, of increasing finite size ε, these quantities are plotted in Figure 8. As expected, the value of $\mathcal{T}_1$ and therefore the cost functional $\mathcal{J}_{\mathrm{main}}$ diverge from their asymptotic values as ε increases. Nevertheless, as summarized in Table 2, the ellipse parametrized by $(\varphi^{\mathrm{opt}}, \gamma^{\mathrm{opt}})$ gives significantly better results (lower values of $\mathcal{T}_1$ and $\mathcal{J}_{\mathrm{main}}$) than a disk or an arbitrarily chosen ellipse with equal surface ratio, also represented in Figure 8.

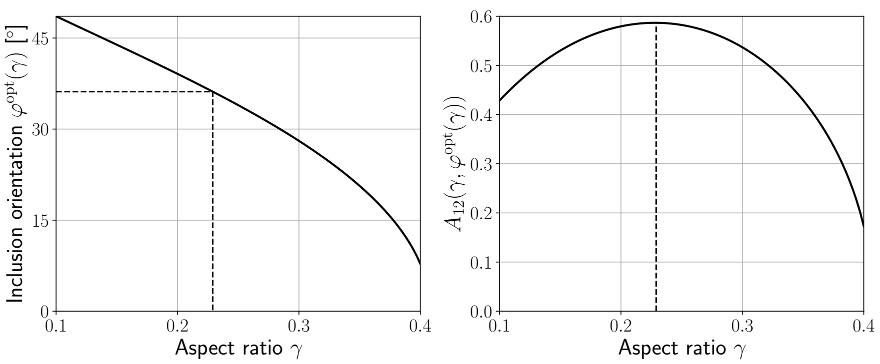

FIG. 7. *Left: Curve $\varphi(\gamma)$ corresponding to $\mathcal{T}_1(\theta_{\mathrm{I}} = 0) = o(\varepsilon^2)$. Right: Coefficient A_{12}, i.e., leading-order contribution of $\partial_\theta \mathcal{T}_1(\theta_{\mathrm{I}} = 0)$, along this curve. Positions of the optimal parameters $(\varphi^{\mathrm{opt}}, \gamma^{\mathrm{opt}})$ are given in dashed lines.*

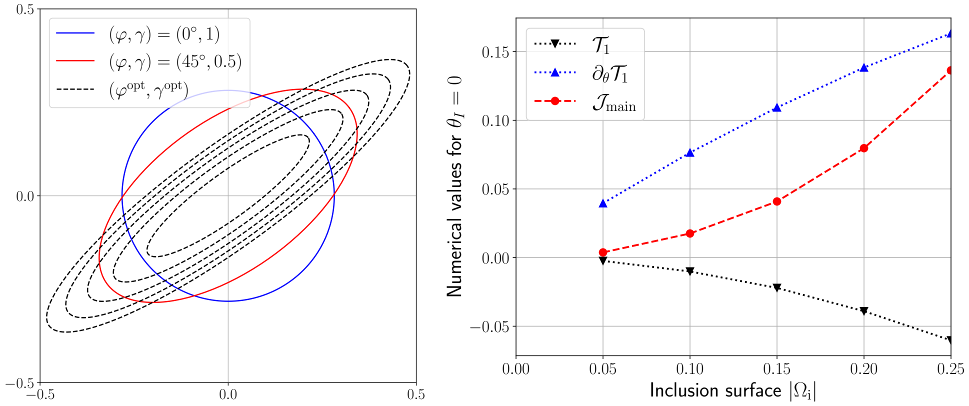

FIG. 8. *Left: Investigated ellipses. Test cases with surface $|\Omega_i| = 0.25$ and "optimal" ellipses for normal incidence $\theta_{\mathrm{I}} = 0$ with increasing surfaces $|\Omega_i| \in \{0.05, 0.25\}$. Right: Values of $\mathcal{T}_1$, $\partial_\theta \mathcal{T}_1$, and $\mathcal{J}_{\mathrm{main}}$, computed numerically for these "optimal" ellipses.*

TABLE 2

Case $\theta_\mathrm{I} = 0$ (normal incidence). Values of functions $\mathcal{T}_1$, $\partial_\theta \mathcal{T}_1$, and $\mathcal{J}_\mathrm{main}$ for several ellipses with the same surface $|\Omega_i| = 0.25$; see Figure 8*. For the disk, one has $\mathcal{B}_2 = 0$ and therefore $\partial_\theta \mathcal{T}_1 = 0$, so that $\mathcal{J}_\mathrm{main}$ is not defined.*

Ellipse	$\mathcal{T}_1$	$\partial_\theta \mathcal{T}_1$	$\mathcal{J}_\mathrm{main} = (\mathcal{T}_1/\partial_\theta \mathcal{T}_1)^2$
$(\varphi,\gamma) = (0°, 1)$ (disk)	-0.11	0	$\emptyset$
$(\varphi,\gamma) = (45°, 0.5)$	-0.10	$8.6 \times 10^{-}2$	1.4
$(\varphi^\mathrm{opt},\gamma^\mathrm{opt}) \approx (36°, 0.23)$	-0.06	0.16	0.14

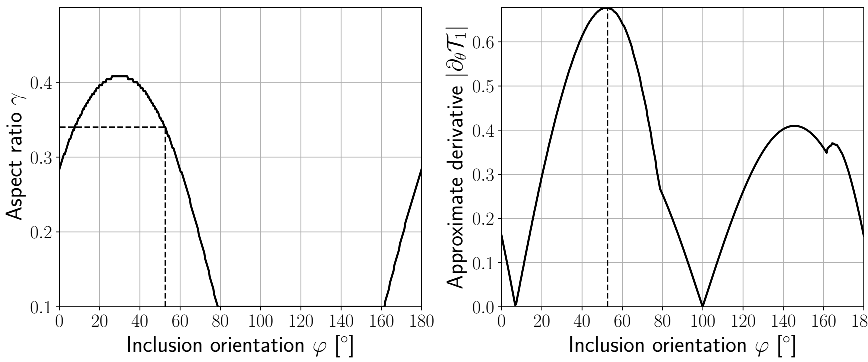

FIG. 9. *Case $\theta_\mathrm{I} = 30°$. Pairs (φ,γ) that achieve $\mathcal{T}_1 = o(\varepsilon^2)$ (left), corresponding leading-order approximation of $\partial_\theta \mathcal{T}_1$ (right), and numerical extraction of the optimal parameters $(\varphi^\mathrm{opt},\gamma^\mathrm{opt}) \approx (53°, 0.34)$ (dashed lines).*

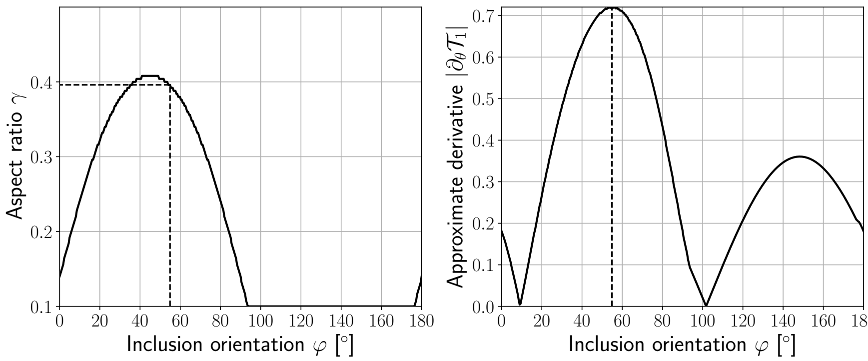

FIG. 10. *Case $\theta_\mathrm{I} = 45°$. Pairs (φ,γ) that achieve $\mathcal{T}_1 = o(\varepsilon^2)$ (left), corresponding leading-order approximation of $\partial_\theta \mathcal{T}_1$ (right), and numerical extraction of the optimal parameters $(\varphi^\mathrm{opt},\gamma^\mathrm{opt}) \approx (55°, 0.40)$ (dashed lines).*

This asymptotic analysis therefore provides a good initial guess that can be used for topological optimization procedures, as seen in the next section.

4.3. Arbitrary incidence: Numerical optimum. For an arbitrary incidence angle θ_I, closed-form expressions for an optimal pair such as (4.6) and (4.7) would be too tedious to obtain. However, the asymptotic approximation of $\mathcal{T}_1(\theta_\mathrm{I})$ as a function of (φ,γ) can easily be computed numerically.

As illustrated in Figures 9 and 10 for $\theta_\mathrm{I} = 30°$ and $\theta_\mathrm{I} = 45°$, respectively, the curves (φ,γ) that achieve $\mathcal{T}_1 = o(\varepsilon^2)$ are numerically extracted, the leading-order approximation of $\partial_\theta \mathcal{T}_1(\theta_\mathrm{I})$ is computed along them, and an optimal pair is determined, similarly to the case $\theta_\mathrm{I} = 0$.

TABLE 3

Case $\theta_{\mathrm{I}} = 30°$. Values of functions $\mathcal{T}_1$, $\partial_\theta \mathcal{T}_1$, and $\mathcal{J}_{\mathrm{main}}$ for several ellipses with the same surface $|\Omega_i| = 0.25$.

Ellipse	$\mathcal{T}_1$	$\partial_\theta \mathcal{T}_1$	$\mathcal{J}_{\mathrm{main}} = (\mathcal{T}_1/\partial_\theta \mathcal{T}_1)^2$
$(\varphi,\gamma) = (0°,1)$ (disk)	-0.11	0.05	4.8
$(\varphi,\gamma) = (45°,0.5)$	-0.055	0.11	0.26
$(\varphi^{\mathrm{opt}},\gamma^{\mathrm{opt}}) \approx (52°,0.34)$	-0.019	0.17	0.012

TABLE 4

Case $\theta_{\mathrm{I}} = 45°$. Values of functions $\mathcal{T}_1$, $\partial_\theta \mathcal{T}_1$, and $\mathcal{J}_{\mathrm{main}}$ for several ellipses with the same surface $|\Omega_i| = 0.25$.

Ellipse	$\mathcal{T}_1$	$\partial_\theta \mathcal{T}_1$	$\mathcal{J}_{\mathrm{main}} = (\mathcal{T}_1/\partial_\theta \mathcal{T}_1)^2$
$(\varphi,\gamma) = (0°,1)$ (disk)	-0.11	0.078	1.8
$(\varphi,\gamma) = (45°,0.5)$	-0.022	0.14	0.025
$(\varphi^{\mathrm{opt}},\gamma^{\mathrm{opt}}) \approx (55°,0.4)$	-0.013	0.16	0.0065

For an ellipse with these characteristics and surface $|\Omega_i| = 0.25$, the values of $\mathcal{T}_1$, $\partial_\theta \mathcal{T}_1$, and $\mathcal{J}_{\mathrm{main}}$ are then computed by numerically solving the cell problems and are compared with the two other ellipses represented in Figure 8. Tables 3 and 4 summarize the results. In these two cases, the “asymptotically optimal” ellipse gives much better results than the two other test cases.

5. Topological optimization of microstructured interfaces. While in the previous section we used the analytical information given by the topological derivative to analyze the case of a unique elliptic inclusion, the aim in this section is to use the topological derivative in an optimization algorithm to minimize a functional with no a priori on the geometry of the inclusion. The efficiency of both methodologies will be investigated through numerical examples in section 5.3.

One aims at generating a microstructure minimizing an objective cost functional $\mathcal{J}(\boldsymbol{m}_{\mathrm{eff}})$ composed of both a main function, for example, (2.27), and some geometrical constraints. An optimal microstructrure is defined by the phase distribution $\boldsymbol{m}_{\mathrm{opt}}$ in the bounded cell Ω^a. The cost functional depends on the macroscopic behavior which is described by the effective parameters $\boldsymbol{m}_{\mathrm{eff}}$ (2.15) that themselves depend on $\boldsymbol{m}$ based on the homogenized model. We therefore consider the following optimization problem:

$$\text{(5.1)} \qquad \text{Find} \qquad \boldsymbol{m}_{\mathrm{opt}} = \arg\min_{\boldsymbol{m}} \tilde{\mathcal{J}}(\boldsymbol{m}) \qquad \text{with} \qquad \tilde{\mathcal{J}}(\boldsymbol{m}) = \mathcal{J}(\boldsymbol{m}_{\mathrm{eff}}).$$

In this context, and given the optimization problem (5.1), one looks for the topological derivative $\mathcal{D}\tilde{\mathcal{J}}$. If $\mathcal{J}$ is differentiable with respect to the effective parameters, $\mathcal{D}\tilde{\mathcal{J}}$ is computed thanks to the chain rule:

$$\text{(5.2)} \qquad \mathcal{D}\tilde{\mathcal{J}} = \frac{\partial \mathcal{J}}{\partial \mathcal{B}} \mathcal{D}\mathcal{B} + \frac{\partial \mathcal{J}}{\partial \mathcal{B}_2} \mathcal{D}\mathcal{B}_2 + \frac{\partial \mathcal{J}}{\partial \mathcal{S}} \mathcal{D}\mathcal{S} + \frac{\partial \mathcal{J}}{\partial \mathcal{C}_1} \mathcal{D}\mathcal{C}_1 + \frac{\partial \mathcal{J}}{\partial \mathcal{C}} \mathcal{D}\mathcal{C}.$$

The final objective is to have at hand a minimization algorithm in order to compute one optimized material distribution in the sense of (5.1).

5.1. Optimization scheme.

5.1.1. FFT-based computation of the cell problems. In order to perform topological optimization, multiple computations of the problem (2.10) are required. Accurately solving this problem with numerical efficiency is therefore crucial. This problem has been tackled in [18] by (i) reformulating the original problem (A.1) derived in [30] and posed in an infinite "strip" into the problem (2.10) posed in a bounded cell (as recalled in Appendix A), and then (ii) decomposing the solution of this equivalent bounded problem as follows:

$$\boldsymbol{\Phi} = \boldsymbol{\Phi}_{\mathrm{per}} + \boldsymbol{\Phi}_{\mathrm{bound}}. \tag{5.3}$$

The two terms of this decomposition are as follows:

- The biperiodic function $\boldsymbol{\Phi}_{\mathrm{per}}$ that satisfies

  $$\boldsymbol{\nabla}\cdot\left(\mu(\boldsymbol{y})\left(\boldsymbol{I}_2+\boldsymbol{\nabla}\boldsymbol{\Phi}_{\mathrm{bound}}+\boldsymbol{\nabla}\boldsymbol{\Phi}_{\mathrm{per}}\right)\right)=\boldsymbol{0} \text{ in } \Omega^a, \tag{5.4}$$

  together with $\int_{\Omega^a}\boldsymbol{\Phi}_{\mathrm{per}}=\boldsymbol{0}$ for uniqueness. This is a usual cell problem, which appears in homogenization of biperiodic media, with a source term that is given by $\boldsymbol{I}_2+\boldsymbol{\nabla}\boldsymbol{\Phi}_{\mathrm{bound}}$.
- The boundary corrector $\boldsymbol{\Phi}_{\mathrm{bound}}$ that is y_2-periodic and ensures that the boundary conditions associated to the DtN conditions in (2.10) are satisfied by imposing

  $$\left(\partial_{\boldsymbol{n}}-\boldsymbol{\Lambda}\right)\boldsymbol{\Phi}_{\mathrm{bound}}\left(\pm\frac{a}{2h},\cdot\right)=-\left(\partial_{\boldsymbol{n}}-\boldsymbol{\Lambda}\right)\boldsymbol{\Phi}_{\mathrm{per}}\left(\pm\frac{a}{2h},\cdot\right). \tag{5.5}$$

The problem is then solved using a fixed-point algorithm specified in [18, section 3.1] and summarized here for completeness.

1. Fix $\boldsymbol{\Phi}^{(0)}_{\mathrm{bound}}=\boldsymbol{0}$.
2. Step $n\to n+1$: given $\boldsymbol{\Phi}^{(n)}_{\mathrm{bound}}$,
   (a) Compute $\boldsymbol{\Phi}^{(n+1)}_{\mathrm{per}}$ by solving the problem (5.4), with the source term given by $\boldsymbol{\Phi}^{(n)}_{\mathrm{bound}}$
   (b) Choose a corrector $\boldsymbol{\Phi}^{(n+1)}_{\mathrm{bound}}$ that satisfies (5.5) (an example of choice is given in [18, section 3.2])
   (c) Compute $\boldsymbol{\Phi}^{(n+1)}=\boldsymbol{\Phi}^{(n+1)}_{\mathrm{per}}+\boldsymbol{\Phi}^{(n+1)}_{\mathrm{bound}}$
3. End when

   $$\frac{||\boldsymbol{\Phi}^{(n+1)}-\boldsymbol{\Phi}^{(n)}||_{L^2(\Omega^a)}}{||\boldsymbol{\Phi}^{(n)}||_{L^2(\Omega^a)}}<\delta_{\mathrm{FP}} \tag{5.6}$$

   with δ_{FP} a user-chosen tolerance.

In practice, the fields are discretized on a regular $N_1\times N_2$ pixel grid mapping the inner cell Ω^a, and a Fourier-based solver is used for step 2(a), that ensures the periodicity requirements on the fields and relies on FFT for efficiency, following [33]. This algorithm has not been investigated theoretically but has been observed to converge in practice.

5.1.2. Material updating. In the configuration mentioned in the introduction, there are only two phases: Ω_m, which is the homogeneous matrix outside the microstructured array, and $\Omega_{\mathrm{i}}\subset\Omega^a$, which is the inclusion phase. Consequently the only material modification allowed in the optimization process is a phase swapping from $(\rho_{\mathrm{i}},\mu_{\mathrm{i}})$ to $(\rho_{\mathrm{m}},\mu_{\mathrm{m}})$ or conversely. Accordingly, the material perturbation $\boldsymbol{\Delta m}$ in the topological derivatives of Proposition 3.23 is chosen as

$$\boldsymbol{\Delta m}=(\rho_{\mathrm{i}}-\rho_{\mathrm{m}},\mu_{\mathrm{i}}-\mu_{\mathrm{m}}) \text{ in } \Omega_m \quad\text{and}\quad \boldsymbol{\Delta m}=(\rho_{\mathrm{m}}-\rho_{\mathrm{i}},\mu_{\mathrm{m}}-\mu_{\mathrm{i}}) \text{ in } \Omega_{\mathrm{i}}. \tag{5.7}$$

Moreover, the shape of the perturbation $\mathcal{P}$ is a disk so that the expression of the polarization tensor is given by (3.27) with $\gamma=1$. The use of the boundary corrector approach described above requires that the phase at the boundaries $y_1=\pm\frac{a}{2h}$ is Ω_m. Consequently, one defines an optimization domain

$$\Omega^{\text{design}} = [-b;b] \times [-1/2;1/2] \quad \text{with} \quad b < \frac{a}{2h}$$

in which material updates are allowed. Since the material is made of two phases, a common way to characterize it is to use a *level-set* function Ψ that satisfies

$$\begin{cases} \Psi(\boldsymbol{z}) > 0 \text{ in } \Omega^{\text{design}} \cap \Omega_m \\ \Psi(\boldsymbol{z}) < 0 \text{ in } \Omega^{\text{design}} \cap \Omega_{\text{i}} \end{cases} \quad \text{and} \quad ||\Psi||_{L^2(\Omega^{\text{design}})} = 1. \tag{5.8}$$

A projection algorithm introduced in [8] for topological optimization can then be used [5, 9, 39, 24]. The main steps are recalled in this subsection.

First, one defines a signed normalized topological derivative $\overline{\mathcal{DJ}}^{(n)}$ at iteration n as

$$\overline{\mathcal{DJ}}^{(n)}(\boldsymbol{z}) = \begin{cases} \mathcal{DJ}^{(n)}(\boldsymbol{z})/||\mathcal{DJ}^{(n)}||_{L^2(\Omega^{\text{design}})} \text{ in } \Omega^{\text{design}} \cap \Omega_m \\ -\mathcal{DJ}^{(n)}(\boldsymbol{z})/||\mathcal{DJ}^{(n)}||_{L^2(\Omega^{\text{design}})} \text{ in } \Omega^{\text{design}} \cap \Omega_{\text{i}}. \end{cases} \tag{5.9}$$

When $\overline{\mathcal{DJ}}^{(n)}$ satisfies the sign condition (5.8), then $\mathcal{DJ}^{(n)}(\boldsymbol{z}) > 0$ is satisfied in the whole optimization domain Ω^{design}. Consequently, in this case, the leading-order approximation of the cost functional $\mathcal{J}$ cannot be decreased anymore by a phase change in Ω^{design}. Therefore, $\overline{\mathcal{DJ}}^{(n)}$ satisfying (5.8) is a sufficient optimal condition that ensures that the material configuration corresponds to a local minimum of $\mathcal{J}$. The iterative updating strategy of [8] for Ψ aims at fulfilling this condition. At each iteration, the new level-set function $\Psi^{(n+1)}$ is computed as

$$\Psi^{(n+1)}(\boldsymbol{z}) = \frac{1}{\sin(\Theta^{(n)})} \left[\sin((1-\kappa^{(n)})\Theta^{(n)})\Psi^{(n)}(\boldsymbol{z}) + \sin(\kappa^{(n)}\Theta^{(n)})\overline{\mathcal{DJ}}^{(n)}(\boldsymbol{z}) \right] \tag{5.10}$$

with the angle $\Theta^{(n)}$ being defined by the projection

$$\Theta^{(n)} = \arccos \left(\overline{\mathcal{DJ}}^{(n)}, \Psi^{(n)} \right)_{L^2(\Omega^{\text{design}})}. \tag{5.11}$$

The parameter $\kappa^{(n)}$ in (5.10) is chosen so that the cost functional decreases at each iteration. In practice, it is initialized to $\kappa^{(0)} = 1$ and then at each iteration it is determined down to a minimal value $\kappa_{\min}$ within an inner optimization loop that reads as follows:

1. Initialization to $\kappa^{(n)} = \min(2, \kappa^{(n-1)})$.
2. Compute $\Psi^{(n+1)}(\boldsymbol{z})$ using (5.10).
3. Compute the associated cost functional $\mathcal{J}^{(n+1)}$ (by solving the cell problem and computing relevant effective quantities) and
   - if $\mathcal{J}^{(n+1)} < \mathcal{J}^{(n)}$, end step n,
   - if $\mathcal{J}^{(n+1)} > \mathcal{J}^{(n)}$ and $\kappa^{(n)} > \kappa_{\min}$, set $\kappa^{(n)} = \kappa^{(n)}/2$ and go back to step 2,
   - if $\mathcal{J}^{(n+1)} > \mathcal{J}^{(n)}$ and $\kappa^{(n)} < \kappa_{\min}$, the whole level-set algorithm is stopped: the cost functional cannot be decreased by the level-set projection.

The stopping criterion of the level-set method associated with the updating step (5.10) is set as

$$|\Theta^{(n)}| < \delta_\Theta \tag{5.12}$$

with δ_Θ a user-chosen tolerance parameter.

Remark 5.1. Different initializations are possible for the level-set function $\Psi^{(0)}$. Here we chose to compute it as $f/||f||_{L^2(\Omega^{\text{design}})}$ with f being defined by

$$f(\boldsymbol{z}) = \begin{cases} \bar{\mu} - \mu(\boldsymbol{z}) \text{ if } \mu_{\text{m}} < \mu_{\text{i}}, \\ \mu(\boldsymbol{z}) - \bar{\mu} \text{ if } \mu_{\text{m}} > \mu_{\text{i}}, \end{cases} \tag{5.13}$$

where $\bar{\mu} = (\mu_{\text{m}} + \mu_{\text{i}})/2$.

5.2. Perimeter and surface constraints. One may want to reach a given phase ratio in the microstructure. Consequently, we denote by $\mathcal{A}$ the target surface of phase Ω_{i} in the unit cell, and we now consider the following cost functional:

$$\mathcal{J}_{\text{main}} + \lambda \left(\frac{|\Omega_i|}{\mathcal{A}} - 1 \right)^2, \tag{5.14}$$

where we added a penalization term to tend to satisfy the surface condition. The parameter λ is a user-chosen parameter which is set so that the final configuration is made of an inclusion surface satisfying $|\Omega_i| \in [\mathcal{A} - \mathcal{A}_{\text{err}}; \mathcal{A} + \mathcal{A}_{\text{err}}]$ with $\mathcal{A}_{\text{err}}$ also chosen by the user. An augmented Lagrangian strategy [34] could be carried out but this is beyond the scope of this paper.

Furthermore, for manufacturing purposes, one aims at getting smooth final configurations that would not be necessary obtained if we only minimize the cost functional (5.14). Consequently one wants to minimize the cost functional

$$\mathcal{J}(\boldsymbol{m}_{\text{eff}}) = \mathcal{J}_{\text{main}} + \lambda \left(\frac{|\Omega_i|}{\mathcal{A}} - 1 \right)^2 + \alpha_{\text{per}} \text{Per}(\Omega_{\text{i}}) \tag{5.15}$$

with $\text{Per}(\Omega_{\text{i}}) = \int_{\partial\Omega_{\text{i}}} \mathrm{d}\sigma$ the perimeter of the inclusions phase in a unit cell and α_{per} a user-chosen parameter. In [6], a regularized perimeter functional Per_ϵ has been introduced to take into account perimeter minimization in topology optimization. This functional has been proved to converge to the exact perimeter as the regularization parameter ϵ tends to 0. In practice, the main idea is to solve sequentially the following approximate problems for $n = 1, \dots, N_{\text{per}}$:

$$\min \mathcal{J}_{\epsilon_n} := \mathcal{J}_{\text{main}} + \lambda \left(\frac{|\Omega_i|}{\mathcal{A}} - 1 \right)^2 + \alpha_{\text{per}} \text{Per}_{\epsilon_n}(\Omega_{\text{i}}) \tag{5.16}$$

with $\epsilon_{n+1} = \epsilon_n/2$, while ϵ_0 and N_{per} are user-chosen parameters. In numerical examples, both λ and α_{per} are user-chosen parameters we can play with in order to find a balance between decreasing $\mathcal{J}_{\text{main}}$, satisfying the volume constraint, and getting smooth final configurations (see [46] for comparisons of final configurations with and without perimeter penalization).

5.3. Numerical examples. In this section, the desired macroscopic effect is to minimize the fields along a given direction θ_{min} with (r, θ) the polar coordinates centered at $\boldsymbol{X_S} = (-35, 0)$, where the source (2.20) is located. It can been visualized as minimizing the cumulative energy (2.21) along a given direction θ_{min}. Following the discussion of section 2.2.2, we then want to have a change of sign for $\mathcal{T}_1$ at θ_{min}. We consequently minimize the regularized cost functional (5.16). The physical parameters are still the ones typical of steel in concrete given by Table 1, while the numerical parameters are given in Table 5.

Table 5
Numerical parameters.

$\kappa_{\min}$	δ_Θ	N_1	N_2	δ_{FP}	ϵ_0	N_{per}
10^{-3}	10^{-1}	101	101	10^{-3}	1	10

In a first example, we chose $\theta_{\mathrm{I}} = 0$ with a surface $\mathcal{A} = 0.2$. In the cost functional (5.16) the coefficients for the surface penalization λ and the perimeter penalization α_{per} are chosen so that $\mathcal{A}_{\mathrm{err}} = 0.06$. Their values for each test case are given in Table 6. Four different initializations are chosen: an ellipse of semiaxes lengths $(0.15, 0.3)$ and tilted of $-\pi/4$, the same ellipse but tilted of $\pi/4$, a random initialization with the same ratio of both materials, and the "asymptotically optimal ellipse" determined in section 4. The initial configurations, the final configurations obtained after the optimization process, and the maps of the cumulative energy (2.21) associated with the effective final configurations are plotted for these four cases in Figure 11. The initial and final values of the cost functional are also given in Tables 6 and 7, respectively. We recover the symmetry of the configuration between the first two cases. We observe that the cost functional is well decreased in every example, so we reach a better configuration by topological optimization than with the optimal ellipse. In addition, it seems that the number of iterations and the value of the cost functional are smaller when we initialize by this asymptotically optimal ellipse, so this can be considered as a valuable initialization to improve the results of the topological optimization process.

A second example for $\theta_{\mathrm{I}} = \pi/4$, $\mathcal{A} = 0.3$, and $\mathcal{A}_{\mathrm{err}} = 0.06$ is described by Table 8, Table 9, and Figure 12. It confirms that the topological optimization algorithm decreases the cost functional. However, for the first two initializations the target angle of $\pi/4$ does not seem to be reached so accurately, as can be noticed in Figures 12(c) and 12(f). In this case, initializing by the optimal ellipse seems even more relevant since the result obtained in Figure 12(i) is more satisfying, with a cost functional and a number of iterations which are lower than for the other initializations. In both examples, although the values of $\mathcal{J}_{\mathrm{main}}$ in the end are significantly lower than the starting ones, the values achieved starting from different initializations are also considerably different. This is due to the presence of multiple local minima and has already been observed for the volume case [17]. This therefore underlines the importance of a good initialization, as the one provided by the optimal ellipse.

Finally, for a better visualization of the optimal periodic microstructures obtained by repeating the unit cells, four of them are displayed in Figure 13.

6. Conclusion.

In this work, formulas are derived for the sensitivities of the homogenized model that describes the propagation of low-frequency scalar waves through a row of inclusions embedded in a homogeneous matrix. To do so, we consider asymptotic expansions for a unit cell where a perturbation is introduced. The expression of the sought topological derivatives of the effective parameters involves the solution of band cell problems in an unperturbed unit cell, and the usual polarization tensor. The numerical computation of these band cell problems had been tackled in a previous work, while the polarization tensor is known analytically for elliptic perturbations, for example. The expression of the topological derivatives are validated numerically and used to perform an analytical analysis of the sensitivity of the model when considering elliptic inclusions. Then a topological optimization process is developed to minimize a proposed cost functional, whose objective is to minimize the

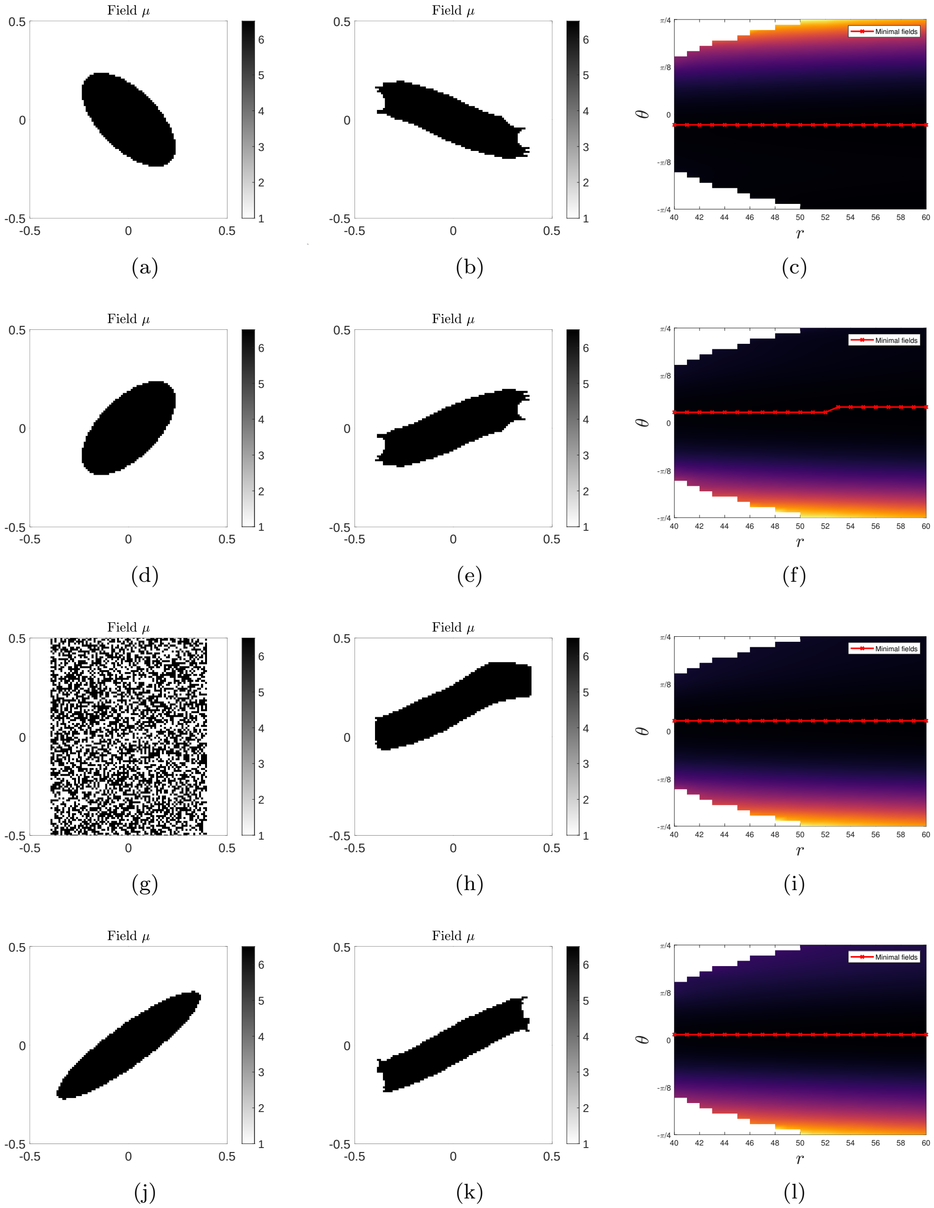

(a) (b) (c)

(d) (e) (f)

(g) (h) (i)

(j) (k) (l)

FIG. 11. *Test cases for* $\theta_{\mathrm{I}} = 0$ *and* $\mathcal{A} = 0.2$. *From left to right columns: initial configuration, final configuration, and local cumulative energy* (2.21) *in the effective medium associated to the final configuration where the position of the minimal value for a given* r *is denoted by the red crosses.*

transmitted fields along a given direction. The material distribution is updated at each iteration thanks to a level-set method and using the topological derivatives obtained in the first part. Surface and perimeter constraints are also added to the cost functional in order to reach local minima that are smoother and avoid trivial solutions.

This study sets a framework for the optimization of microstructured interfaces based on their homogenized properties. This work could be extended to other configurations, such as the following:

TABLE 6

Initial values for the different configurations with objective $\theta_{\mathrm{I}} = 0$ presented in Figure 11: surface and perimeter parameters, and values of functionals before optimization.

	λ	α_{per}	$\mathcal{J}$ init.	$\mathcal{J}_{\mathrm{main}}$ init.
ellipse $(0.15, 0.3, -\pi/4)$	0.5	0.2	1.21	$9.72 \cdot 10^{-1}$
ellipse $(0.15, 0.3, \pi/4)$	0.5	0.2	1.21	$9.72 \cdot 10^{-1}$
random	0.5	0.2	$5.23 \cdot 10^{3}$	$5.23 \cdot 10^{3}$
optimal ellipse	0.15	$5 \cdot 10^{-2}$	$1.02 \cdot 10^{-1}$	$3.61 \cdot 10^{-1}$

TABLE 7

Final values for the different configurations with objective $\theta_{\mathrm{I}} = 0$ presented in Figure 11: number of iterations, final surface, and values of functionals after optimization.

	N_{iter}	$\lvert\Omega_i\rvert$ end	$\mathcal{J}$ end	$\mathcal{J}_{\mathrm{main}}$ end
ellipse $(0.15, 0.3, -\pi/4)$	103	0.15	$2.24 \cdot 10^{-1}$	$1.4 \cdot 10^{-2}$
ellipse $(0.15, 0.3, \pi/4)$	103	0.15	$2.24 \cdot 10^{-1}$	$1.4 \cdot 10^{-2}$
random	82	0.16	$1.93 \cdot 10^{-1}$	$7.2 \cdot 10^{-3}$
optimal ellipse	60	0.14	$6.76 \cdot 10^{-2}$	$2.1 \cdot 10^{-3}$

TABLE 8

Initial values for the different configurations with objective $\theta_{\mathrm{I}} = \pi/4$ presented in Figure 12: surface and perimeter parameters, and values of functionals before optimization.

	λ	α_{per}	$\mathcal{J}$ init.	$\mathcal{J}_{\mathrm{main}}$ init.
ellipse $(0.15, 0.3, \pi/4)$	0.3	$7 \cdot 10^{-2}$	1.51	1.40
random	1	$1 \cdot 10^{-1}$	$2.03 \cdot 10^{-1}$	$2.11 \cdot 10^{-4}$
optimal ellipse	0.3	$7 \cdot 10^{-2}$	$6.27 \cdot 10^{-2}$	$3.30 \cdot 10^{-3}$

TABLE 9

Final values for the different configurations with objective $\theta_{\mathrm{I}} = \pi/4$ presented in Figure 12: number of iterations, final surface, and values of functionals after optimization.

	N_{iter}	$\lvert\Omega_i\rvert$ end	$\mathcal{J}$ end	$\mathcal{J}_{\mathrm{main}}$ end
ellipse $(0.15, 0.3, \pi/4)$	49	0.30	$2.84 \cdot 10^{-2}$	$9.72 \cdot 10^{-5}$
random	52	0.24	$1.35 \cdot 10^{-1}$	$7.99 \cdot 10^{-4}$
optimal ellipse	28	0.28	$2.96 \cdot 10^{-2}$	$8.76 \cdot 10^{-5}$

- Resonant interfaces, obtained, e.g., for highly contrasted inclusions [48, 47]. In this case, frequency-dependent coefficients have been derived, and while homogenization-based optimization procedures exist for fully periodic resonant media, e.g., [49], they are quite scarce for such interfaces, to the best of our knowledge.
- High-frequency behavior. Again, the specific homogenization procedure for higher frequencies or shorter wavelengths is well-known for fully periodic media and has been used for optimization [37], but could be extended to interfaces.
- *Graded* metasurfaces. By relaxing the periodicity assumption and allowing for slow variations of the periodicity cell size along the interface, one may obtain graded interfaces (sometimes called *quasi-periodic* [41]) able to produce stronger macroscopic effects than their strictly periodic counterparts. Optimization procedures also exist for such configurations [35].
- Other physical contexts. The scalar wave equation adressed in this study is quite general already and may model acoustics, antiplane shear elastic waves, or transversely polarized electromagnetic waves. Extensions to (vector-valued) Maxwell or elasticity equations are however possible within the same

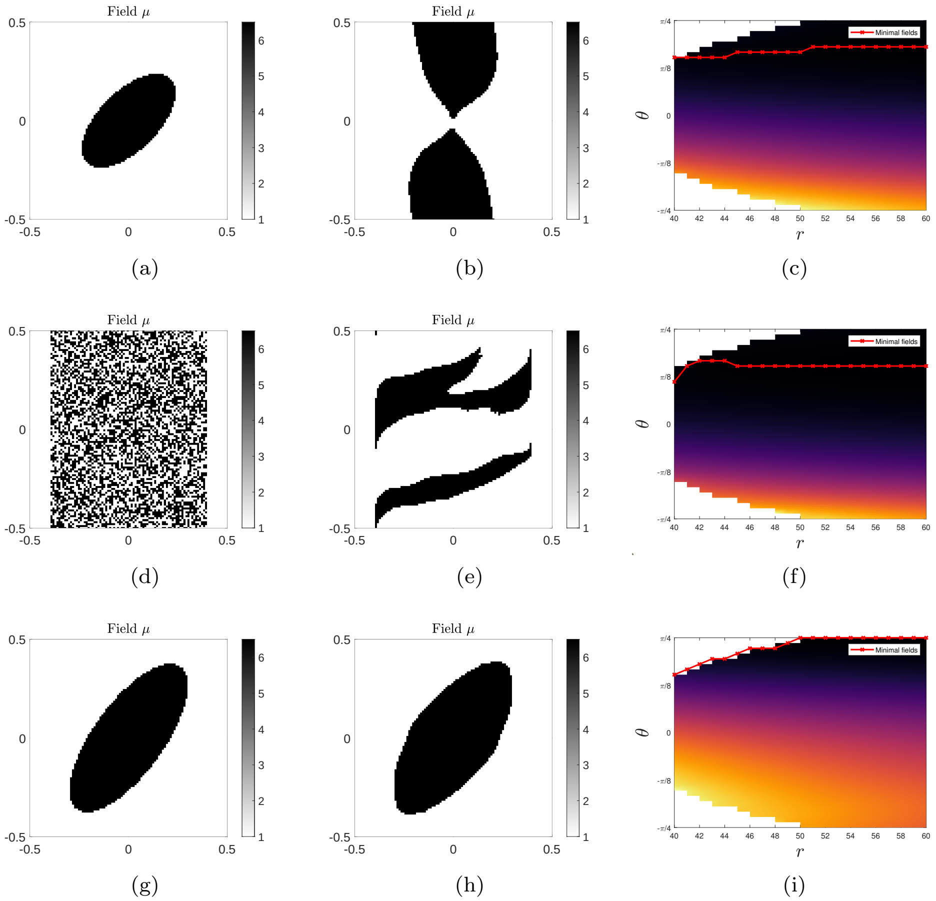

FIG. 12. *Test cases for* $\theta_{\mathrm{I}} = \pi/4$ *and* $\mathcal{A} = 0.3$. *From left to right columns: initial configuration, final configuration, and local cumulative energy* (2.21) *in the effective medium associated to the final configuration where the position of the minimal value for a given* r *is denoted by the red crosses.*

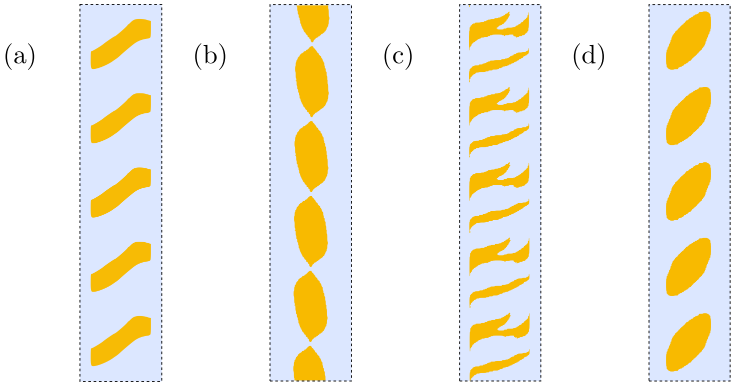

FIG. 13. *Final microstructures corresponding to the optimal cells displayed in Figures* (a) 11*h*, (b) 12*b*, (c) 12*e*, *and* (d) 12*h*.

matched asymtotics framework (see [43] for a related study) and would open the way of optimization procedures for macroscopic effects typical of vector-valued wave problems such as mode conversion at the interface (e.g., P-waves to S-waves for isotropic elasticity).

Appendix A. Dirichlet-to-Neumann operator. In this section, the steps used in [18] to obtain the cell problem (2.10) with DtN boundary conditions are briefly recalled. The problem initially derived in [30], posed in the infinite strip Ω, reads

$$\begin{cases} \boldsymbol{\nabla}\cdot\left(\mu(\boldsymbol{y})\left(\boldsymbol{\nabla_y}\boldsymbol{\Phi}(\boldsymbol{y})+\boldsymbol{I}_2\right)\right)=\mathbf{0} \text{ in } \Omega, \\ \mu(\boldsymbol{y})[\boldsymbol{\nabla_y}\boldsymbol{\Phi}(\boldsymbol{y})+\boldsymbol{I}_2]\cdot\boldsymbol{n} \text{ and } \boldsymbol{\Phi} \text{ are continuous on } \partial\Omega_{\mathrm{i}}, \\ \boldsymbol{\Phi} \text{ is } y_2\text{-periodic}, \\ \displaystyle\lim_{y_1\to\pm\infty}\boldsymbol{\nabla_y}\boldsymbol{\Phi}(y_1,y_2)=\mathbf{0}. \end{cases} \tag{A.1}$$

The variations of the physical parameters are restricted to Ω^a due to its definition in (2.7). Introducing the half-strips $\Omega_a^+=[\frac{a}{2h},+\infty[\times I$ and $\Omega_a^- =]-\infty,-\frac{a}{2h}]\times I$ (see Figure 2), the restrictions $\boldsymbol{\Phi}^\pm := \boldsymbol{\Phi}_{|\Omega_a^\pm}$ satisfy $\boldsymbol{\Delta}\boldsymbol{\Phi}^\pm=\mathbf{0}$ in $\Omega_a^\pm$, along with the periodicity and decaying conditions. The modal decomposition of these fields, classically found in the literature on waveguides [26, 15] and also used in [30] to find approximate solutions, then reads

$$\boldsymbol{\Phi}^\pm(y_1,y_2)=\sum_{n\in\mathbb{Z}}\boldsymbol{\Phi}_n^\pm \mathrm{e}^{\mp|\xi_n|\left(y_1\mp\frac{a}{2h}\right)}\Psi_n(y_2) \text{ with } \quad \Psi_n(y_2)=\mathrm{e}^{\mathrm{i}\xi_n y_2},\ \xi_n=2n\pi. \tag{A.2}$$

The modes $\{\Psi_n\}$ are orthonormal for the L^2 scalar product $(\cdot,\cdot)_{\mathrm{I}}$ on any vertical section I, i.e., they satisfy

$$(\Psi_p,\Psi_q)_{\mathrm{I}}=\delta_{pq} \text{ with } (f,g)_{\mathrm{I}}:=\int_I f(y_2)\overline{g(y_2)}\mathrm{d}y_2. \tag{A.3}$$

Consequently, choosing the particular section $I^+=\{(y_1,y_2)\in\Omega_a^+,\, y_1=\frac{a}{2h}\}$ (see Figure 2) yields the expression of the modal coefficients in the right half-strip:

$$\boldsymbol{\Phi}_n^+=\left(\boldsymbol{\Phi}^+\left(\frac{a}{2h},\cdot\right),\Psi_n\right)_I=\int_I\boldsymbol{\Phi}^+\left(\frac{a}{2h},y_2\right)\overline{\Psi_n(y_2)}\mathrm{d}y_2. \tag{A.4}$$

One differentiates the decomposition (A.2) with respect to y_1 and uses the expression of the coefficients (A.4) to get the following DtN operator linking the traces of $\boldsymbol{\Phi}$ and of its normal derivative on the section I^+ where $\boldsymbol{\Phi}=\boldsymbol{\Phi}^+$:

$$\partial_{y_1}\boldsymbol{\Phi}\left(\frac{a}{2h},\cdot\right)=\boldsymbol{\Lambda}\left[\boldsymbol{\Phi}\left(\frac{a}{2h},\cdot\right)\right] \text{ with } \boldsymbol{\Lambda}[\boldsymbol{f}](y_2)=-\sum_{n\in\mathbb{Z}}(\boldsymbol{f},\Psi_n)_{\mathrm{I}}|\xi_n|\Psi_n(y_2). \tag{A.5}$$

Similarly, focusing on the particular section $I^-=\{(y_1,y_2)\in\Omega_a^-,\, y_1=-\frac{a}{2h}\}$ (see Figure 2) provides the expression of the "left" modal coefficients of $\boldsymbol{\Phi}^-$. The DtN relation is finally found to be the same for both interfaces $I^\pm$, up to the direction of the outer normal derivative:

$$\partial_{\boldsymbol{n}}\boldsymbol{\Phi}\left(\pm\frac{a}{2h},\cdot\right)=\boldsymbol{\Lambda}\left[\boldsymbol{\Phi}\left(\pm\frac{a}{2h},\cdot\right)\right], \quad \text{where } \partial_{\boldsymbol{n}}=\pm\partial y_1. \tag{A.6}$$

The problem posed in the infinite band (A.1) can thus be rewritten as the problem (2.10) with DtN boundary conditions on the bounded cell (2.7).

Appendix B. Properties of Green's functions. The definition of the full-space fundamental solution G_∞ in (3.9) implies

$$-\mu_\star \Delta_{\boldsymbol{r}} G_\infty(\boldsymbol{r};\mu_\star) = \delta(\boldsymbol{r}) \quad \text{and} \quad \boldsymbol{\nabla}_{\boldsymbol{r}} G_\infty(\boldsymbol{r};\mu_\star) = -\frac{\boldsymbol{r}}{2\pi\mu_\star\|\boldsymbol{r}\|^2}. \tag{B.1}$$

From the problem (3.8), the decomposition of the fundamental solution G given in (3.9), and the equalities above, then the complementary part G_c is defined as the solution of the PDE,

$$\begin{aligned}-\boldsymbol{\nabla}_{\boldsymbol{y}} \cdot \left(\frac{\mu(\boldsymbol{y})}{\mu_{\mathrm{m}}} \boldsymbol{\nabla}_{\boldsymbol{y}} G_c(\boldsymbol{y},\boldsymbol{x})\right) &= \boldsymbol{\nabla}_{\boldsymbol{y}} \cdot \left(\frac{\mu(\boldsymbol{y}) - \mu(\boldsymbol{x})}{\mu_{\mathrm{m}}} \boldsymbol{\nabla}_{\boldsymbol{y}} G_\infty\left(\boldsymbol{y}-\boldsymbol{x};\frac{\mu(\boldsymbol{x})}{\mu_{\mathrm{m}}}\right)\right)\\ &= -\boldsymbol{\nabla}_{\boldsymbol{y}} \cdot \left(\frac{[\mu(\boldsymbol{y}) - \mu(\boldsymbol{x})]\,(\boldsymbol{y}-\boldsymbol{x})}{2\pi\mu(\boldsymbol{x})\|\boldsymbol{y}-\boldsymbol{x}\|^2}\right)\end{aligned} \tag{B.2}$$

along with the boundary conditions,

$$G_c(\cdot,\boldsymbol{x}) + G_\infty\left(\cdot - \boldsymbol{x};\frac{\mu(\boldsymbol{x})}{\mu_{\mathrm{m}}}\right) \quad \text{is } y_2\text{-periodic}, \tag{B.3}$$

and

$$-\left(\partial_{\boldsymbol{n}} + \Lambda\right)[G_c(\boldsymbol{y},\boldsymbol{x})]\Big|_{y_1=\pm\frac{a}{2h}} = \left(\partial_{\boldsymbol{n}} + \Lambda\right)\left[G_\infty\left(\boldsymbol{y}-\boldsymbol{x};\frac{\mu(\boldsymbol{x})}{\mu_{\mathrm{m}}}\right)\right]\Big|_{y_1=\pm\frac{a}{2h}} \quad \forall \boldsymbol{y}\in I^\pm. \tag{B.4}$$

The right-hand side of the PDE (B.2) is seen to be regular as $\boldsymbol{y}\to\boldsymbol{x}$ as soon as the material coefficient μ is C^1 in a neighborhood of $\boldsymbol{x}$. Therefore, $G_c(\cdot,\boldsymbol{x})$ and its gradient are ensured to be regular functions when $\boldsymbol{x}$ is itself in the neighborhood of the perturbation point $\boldsymbol{z}$, which is not located on a material interface. Using the rescaled coordinates $(\boldsymbol{y},\boldsymbol{x}) = (\boldsymbol{z}+\varepsilon\bar{\boldsymbol{y}}, \boldsymbol{z}+\varepsilon\bar{\boldsymbol{x}})$, one obtains the asymptotic behavior:

$$\boldsymbol{\nabla}_{\boldsymbol{y}} G_c(\boldsymbol{y},\boldsymbol{x}) = \boldsymbol{\nabla}_{\boldsymbol{y}} G_c(\boldsymbol{z},\boldsymbol{z}) + o(1) = \mathcal{O}(1) \quad \text{as } \varepsilon\to 0. \tag{B.5}$$

REFERENCES

[1] G. Allaire, C. Dapogny, and F. Jouve, *Shape and topology optimization*, in Geometric Partial Differential Equations - Part II, Elsevier, Amsetrdam, 2021, pp. 1–132, https://doi.org/10.1016/bs.hna.2020.10.004.

[2] G. Allaire, F. de Gournay, F. Jouve, and A.-M. Toader, *Structural optimization using topological and shape sensitivity via a level set method*, Control Cybern., 34 (2005), pp. 59–80.

[3] G. Allaire and T. Yamada, *Optimization of dispersive coefficients in the homogenization of the wave equation in periodic structures*, Numer. Math., 140 (2018), pp. 265–326, https://doi.org/10.1007/s00211-018-0972-4.

[4] H. Ammari and H. Kang, *Polarization and Moment Tensors: With Applications to Inverse Problems and Effective Medium Theory*, Appl. Math. Sci. 162, Springer, New York, 2007.

[5] S. Amstutz, *Analysis of a level set method for topology optimization*, Optim. Methods Softw., 26 (2011), pp. 555–573, https://doi.org/10.1080/10556788.2010.521557.

[6] S. Amstutz, *Regularized perimeter for topology optimization*, SIAM J. Control Optim., 51 (2013), pp. 2176–2199, https://doi.org/10.1137/100816997.

[7] S. Amstutz, *An introduction to the topological derivative*, Eng. Comput., 39 (2021), pp. 3–33, https://doi.org/10.1108/ec-07-2021-0433.

[8] S. Amstutz and H. Andrä, *A new algorithm for topology optimization using a level-set method*, J. Comput. Phys., 216 (2006), pp. 573–588, https://doi.org/10.1016/j.jcp.2005.12.015.

[9] S. Amstutz, S. M. Giusti, A. A. Novotny, and E. A. de Souza Neto, *Topological derivative for multi-scale linear elasticity models applied to the synthesis of microstructures*, Internat. J. Numer. Methods Engrg., 84 (2010), pp. 733–756, https://doi.org/10.1002/nme.2922.

[10] B. Assouar, B. Liang, Y. Wu, Y. Li, J.-C. Cheng, and Y. Jing, *Acoustic metasurfaces*, Nat. Rev. Mater., 3 (2018), pp. 460–472, https://doi.org/10.1038/s41578-018-0061-4.

[11] M. P. Bendsøe and O. Sigmund, *Topology Optimization*, Springer, Berlin, 2003.

[12] A. Bensoussan, J.-L. Lions, and G. Papanicolaou, *Asymptotic Analysis for Periodic Structures*, AMS Chelsea, Providence, RI, 2011.

[13] M. Bonnet, *Higher-order topological sensitivity for 2-D potential problems. Application to fast identification of inclusions*, Int. J. Solids Struct., 46 (2009), pp. 2275–2292, https://doi.org/10.1016/j.ijsolstr.2009.01.021.

[14] M. Bonnet, R. Cornaggia, and B. B. Guzina, *Microstructural topological sensitivities of the second-order macroscopic model for waves in periodic media*, SIAM J. Appl. Math., 78 (2018), pp. 2057–2082, https://doi.org/10.1137/17m1149018.

[15] A.-S. Bonnet-Ben Dhia and G. Legendre, *An alternative to Dirichlet-to-Neumann maps for waveguides*, C. R. Math., 349 (2011), pp. 1005–1009, https://doi.org/10.1016/j.crma.2011.08.006.

[16] D. Cedio-Fengya, S. Moskow, and M. Vogelius, *Identification of conductivity imperfections of small diameter by boundary measurements. Continuous dependence and computational reconstruction*, Inverse Problems, 14 (1998), pp. 553–595, https://doi.org/10.1088/0266-5611/14/3/011.

[17] R. Cornaggia and C. Bellis, *Tuning effective dynamical properties of periodic media by FFT-accelerated topological optimization*, Internat. J. Numer. Methods Engrg., 121 (2020), pp. 3178–3205, https://doi.org/10.1002/nme.6352.

[18] R. Cornaggia, M. Touboul, and C. Bellis, *FFT-based computation of homogenized interface parameters*, C. R. Mécanique, 350 (2022), pp. 297–307, https://doi.org/10.5802/crmeca.119.

[19] R. Craster, S. Guenneau, M. Kadic, and M. Wegener, *Mechanical metamaterials*, Rep. Progr. Phys., 86 (2023), 094501, https://doi.org/10.1088/1361-6633/ace069.

[20] M. David, C. Pideri, and J.-J. Marigo, *Homogenized interface model describing inhomogeneities located on a surface*, J. Elasticity, 109 (2012), pp. 153–187, https://doi.org/10.1007/s10659-012-9374-5.

[21] B. Delourme. *Modèles asymptotiques des interfaces fines et périodiques en électromagnétisme*, Ph.D. thesis, Université Pierre et Marie Curie - Paris VI, 2010.

[22] B. Delourme, H. Haddar, and P. Joly, *Approximate models for wave propagation across thin periodic interfaces*, J. Math. Pures Appl., 98 (2012), pp. 28–71.

[23] B. Delourme, E. Lunéville, J.-J. Marigo, A. Maurel, J.-F. Mercier, and K. Pham, *A stable, unified model for resonant Faraday cages*, Proc. A, 477 (2021), 20200668, https://doi.org/10.1098/rspa.2020.0668.

[24] S. Giusti, A. Ferrer, and J. Oliver, *Topological sensitivity analysis in heterogeneous anisotropic elasticity problem. Theoretical and computational aspects*, Comput. Methods Appl. Mech. Engrg., 311 (2016), pp. 134–150, https://doi.org/10.1016/j.cma.2016.08.004.

[25] S. M. Giusti, A. A. Novotny, and E. A. de Souza Neto, *Sensitivity of the macroscopic response of elastic microstructures to the insertion of inclusions*, Proc. A, 466 (2010), pp. 1703–1723, https://doi.org/10.1098/rspa.2009.0499.

[26] I. Harari, I. Patlashenko, and D. Givoli, *Dirichlet-to-Neumann maps for unbounded wave guides*, J. Comput. Phys., 143 (1998), pp. 200–223, https://doi.org/10.1006/jcph.1998.5960.

[27] K. M. Ho, C. K. Cheng, Z. Yang, X. X. Zhang, and P. Sheng, *Broadband locally resonant sonic shields*, Appl. Phys. Lett., 83 (2003), pp. 5566–5568, https://doi.org/10.1063/1.1637152.

[28] B. Lombard, A. Maurel, and J.-J. Marigo, *Numerical modeling of the acoustic wave propagation across an homogenized rigid microstructure in the time domain*, J. Comput. Phys., 335 (2017), pp. 558–577, https://doi.org/10.1016/j.jcp.2017.01.036.

[29] J.-J. Marigo and A. Maurel, *Homogenization models for thin rigid structured surfaces and films*, J. Acoust. Soc. Amer., 140 (2016), pp. 260–273, https://doi.org/10.1121/1.4954756.

[30] J.-J. Marigo, A. Maurel, K. Pham, and A. Sbitti, *Effective dynamic properites of a row of elastic inclusions: The case of scalar shear waves*, J. Elasticity, 128 (2017), pp. 265–289, https://doi.org/10.1007/s10659-017-9627-4.

[31] J.-J. Marigo and C. Pideri, *The effective behaviour of elastic bodies containing microcracks or microholes localized on a surface*, Int. J. Damage Mech., 20 (2011), pp. 1151–1177, https://doi.org/10.1177/1056789511406914.

[32] K. Matsushima, H. Isakari, T. Takahashi, and T. Matsumoto, *A topology optimisation of composite elastic metamaterial slabs based on the manipulation of far-field behaviours*, Struct. Multidiscip. Optim., 63 (2020), pp. 231–243, https://doi.org/10.1007/s00158-020-02689-y.

[33] H. Moulinec and P. Suquet, *A numerical method for computing the overall response of nonlinear composites with complex microstructure*, Comput. Methods Appl. Mech. Engrg., 157 (1998), pp. 69–94, https://doi.org/10.1016/s0045-7825(97)00218-1.

[34] J. Nocedal and S. Wright, *Numerical Optimization*, Springer Ser. Oper. Res. Financ. Eng., Springer, New York, 2006.

[35] Y. Noguchi and T. Yamada, *Level set-based topology optimization for graded acoustic metasurfaces using two-scale homogenization*, Finite Elem. Anal. Des., 196 (2021), 103606, https://doi.org/10.1016/j.finel.2021.103606.

[36] Y. Noguchi and T. Yamada, *Topology optimization of acoustic metasurfaces by using a two-scale homogenization method*, Appl. Math. Model., 98 (2021), pp. 465–497, https://doi.org/10.1016/j.apm.2021.05.005.

[37] Y. Noguchi, T. Yamada, K. Izui, and S. Nishiwaki, *Topology optimization for hyperbolic acoustic metamaterials using a high-frequency homogenization method*, Comput. Methods Appl. Mech. Engrg., 335 (2018), pp. 419–471, https://doi.org/10.1016/j.cma.2018.02.031.

[38] A. A. Novotny and J. Sokołowski, *Topological Derivatives in Shape Optimization*, Springer, Berlin, 2013, https://doi.org/10.1007/978-3-642-35245-4.

[39] J. Oliver, A. Ferrer, J. C. Cante, S. M. Giusti, and O. Lloberas-Valls, *On multiscale computational design of structural materials using the topological derivative*, in Computational Methods in Applied Sciences, Springer, New York, 2017, pp. 289–308, https://doi.org/10.1007/978-3-319-60885-3_14.

[40] W. J. Parnell, *The Eshelby, Hill, moment and concentration tensors for ellipsoidal inhomogeneities in the Newtonian potential problem and linear elastostatics*, J. Elasticity, (2016), pp. 1–64, https://doi.org/10.1007/s10659-016-9573-6.

[41] K. Pham, N. Lebbe, and A. Maurel, *Diffraction grating with varying slit width: Quasiperiodic homogenization and its numerical implementation*, J. Comput. Phys., 473 (2023), 111727, https://doi.org/10.1016/j.jcp.2022.111727.

[42] K. Pham, A. Maurel, and J.-J. Marigo, *Two scale homogenization of a row of locally resonant inclusions - the case of shear waves*, J. Mech. Phys. Solids, 106 (2017), pp. 80–94, https://doi.org/10.1016/j.jmps.2017.05.001.

[43] K. Pham, A. Maurel, and J.-J. Marigo, *Revisiting imperfect interface laws for two-dimensional elastodynamics*, Proc. A, 477 (2021), 20200519, https://doi.org/10.1098/rspa.2020.0519.

[44] E. Sánchez-Palencia, *Non-Homogeneous Media and Vibration Theory*, Lecture Notes in Phys. 127, Springer, New York, 1980.

[45] O. Sigmund, *Materials with prescribed constitutive parameters: An inverse homogenization problem*, Int. J. Solids Struct., 31 (1994), pp. 2313–2329, https://doi.org/10.1016/0020-7683(94)90154-6.

[46] M. Touboul, *Acoustic and Elastic Wave Propagation in Microstructured Media with Interfaces: Homogenization, Simulation and Optimization*, Ph.D. thesis, Aix-Marseille Université, 2021.

[47] M. Touboul, B. Lombard, and C. Bellis, *Time-domain simulation of wave propagation across resonant meta-interfaces*, J. Comput. Phys., 414 (2020), 109474, https://doi.org/10.1016/j.jcp.2020.109474.

[48] M. Touboul, K. Pham, A. Maurel, J.-J. Marigo, B. Lombard, and C. Bellis, *Effective resonant model and simulations in the time-domain of wave scattering from a periodic row of highly-contrasted inclusions*, J. Elasticity, 142 (2020), pp. 53–82, https://doi.org/10.1007/s10659-020-09789-2.

[49] J. Vondřejc, E. Rohan, and J. Heczko, *Shape optimization of phononic band gap structures using the homogenization approach*, Int. J. Solids Struct., 113-114 (2017), pp. 147–168, https://doi.org/10.1016/j.ijsolstr.2017.01.038.